A Modular Multilevel Converter With Active Power Filter for Submodule Capacitor Voltage Ripples and Power Losses Reduction

Guanlong Jia, *Student Member, IEEE*, Min Chen, *Member, IEEE*, Song Tang, *Student Member, IEEE*, Chenghao Zhang, and Bin Zhao

***Abstract*—Modular multilevel converter (MMC) topology has been widely used in the medium-/high-voltage applications. However, large capacitance is needed to suppress submodule (SM) capacitor voltage ripples. This article presents a modified MMC with the active power filter (APF-MMC) paralleled between the *N*th SM of the upper arm and the first SM of the lower arm in each phase without changing the original topology. It is intended to decrease the capacitor voltage fluctuations and power losses of SMs by diverting the phase low-frequency ripple powers into the storage capacitor of the additional active power filter circuit. Both the detailed SM capacitor voltage fluctuations, which can be reduced up to 50% of the original value in the traditional MMC topology, and the SM average currents, which are proportional to SM switching losses and can be reduced up to 87.83% of the original value, are analyzed. The arm rms currents are also derived, which are related to SM conduction losses. Moreover, the operating principle, modulation method, and control strategy are presented in detail. Finally, the APF-MMC and the traditional MMC topology simulation and experimental platforms were built. The simulation and experimental results demonstrate the validity and performance of the APF-MMC topology and control strategy by comparing with the traditional MMC topology.**

***Index Terms*—Active power filter (APF), capacitor voltage ripples, modular multilevel converter (MMC), power losses.**

I. INTRODUCTION

COMPARED with the neutral point clamped converter and the cascaded H-bridge converter, the modular multilevel converter (MMC) has recently received increasing attention in the medium- and high-voltage applications [1]–[3]. The MMC topology was first introduced by Lesnicar and Marquart [4], and it has some prominent advantages, such as modular design, black start-up capability, and high-quality output waveforms [5], [6]. These advantages make the MMC topology considered as one of the promising candidates among numerous high-voltage direct current (HVdc) topologies [7]. And MMC topology has made great success in the HVdc transmission and offshore wind power system, e.g., 200 kV, 400 MVA "Trans Bay Cable Project" by Siemens [8].

For the traditional MMC topology, the energy exchange between the dc side and the ac side is mainly accomplished by the capacitors of the submodules (SMs), which causes voltage fluctuations of the SM capacitors. The fundamental and second-order frequency harmonics are the main components of the voltage fluctuations [9], and the amplitude of each harmonic in SM capacitor voltage fluctuations is proportional to the output current and related to the SM capacitance value. In order to suppress the SM capacitor voltage fluctuations, the larger capacitance value is required [10]. At the same time, the MMC topology requires a large number of SM capacitors, which makes the system bulky and costly. Therefore, the decrease in capacitor voltage ripples is of great significance.

In the recent few years, many studies have been implemented on control strategies and new topologies for reducing the capacitor voltage fluctuations [11]–[23]. In terms of control strategies, in [11], high-order frequency circulating current is injected into each arm to achieve a reduction in the fundamental frequency capacitor voltage fluctuation. Similarly, in [12], a second harmonic is injected into the circulating currents of each phase to reduce the second-order frequency capacitor voltage fluctuation [13]. The injection of a fourth-order frequency circulating current in coordination with the second one is also introduced in [14] and [15]. The main drawbacks of these control strategies are that the calculation of the injected values is complicated and can only be accomplished by a lookup table method [16]. The real-time calculation of circulating current reference is proposed in [17]. However, the calculation result is not accurate because it ignores the power losses and parasitic parameters [18]. Moreover, the injected circulating currents result in great power losses as well as overrating of the power devices in the MMC topology [19].

To avoid the above-mentioned drawbacks of control strategies, a novel MMC topology with a shared SM per phase is introduced in [20], which could reduce the SM number by one for each phase and reduce the voltage ripples of the shared SM. However, except for the shared SM, other SM capacitor voltage ripples are still not reduced. Based on the topology

Manuscript received July 22, 2019; revised October 14, 2019 and January 16, 2020; accepted March 16, 2020. Date of publication March 22, 2020; date of current version July 20, 2020. This work was supported in part by the National Key R&D Program of China under Grant 2017YFB0903100 and in part by the Science and Technology Foundation of State Grid Corporation of China under Grant 521104170043. Recommended for publication by Associate Editor J. Wang. *(Corresponding author: Min Chen.)*

The authors are with the Department of Applied Electronics, Zhejiang University, Hangzhou 310057, China (e-mail: xizhao513196@zju.edu.cn; calim@zju.edu.cn; tangsong718@zju.edu.cn; 3150102973@zju.edu.cn; zhaobin9528@zju.edu.cn).

Color versions of one or more of the figures in this article are available online at http://ieeexplore.ieee.org.

Digital Object Identifier 10.1109/TPEL.2020.2982440

in [20], an improved topology with additionally connecting both the top and the bottom SMs via cables is introduced to reduce the fluctuations [21]. Similarly, except for the shared SM and the SMs connected by cable, other SM capacitor voltage ripples remain unchanged. In order to reduce the capacitor voltage ripples of each SM, an improved topology is proposed [22], which adds a channel between the corresponding upper and lower arm SMs. However, it requires a considerable amount of isolation transformers and cannot reduce the second-order ripple powers. In [10], an active power filter (APF) circuit is added to each SM to transfer all the ripple powers in the SM capacitor to the APF circuit, thereby dramatically reducing the fluctuations of SM capacitor voltage. However, the number of IGBTs and capacitors is roughly two times that of the traditional MMC topology. On the other hand, each SM requires an additional buffer inductor, and the power losses of SMs are increased. In [23], an additional active cross-connected branch is connected between the midpoints of the two arms in each phase of MMC to reduce the capacitor voltage ripples. The AC-MMC topology does not require changes to the traditional MMC topology, and its passive devices can be further reduced [24], but the arm currents are still higher [25], which increases the power losses of the SMs. To reduce the number of additional passive power devices and the power losses of SMs, a novel MMC topology with the three-terminal middle cells inserted per phase is presented in [26], and it is designed to decrease the SM capacitor voltage ripples by controlling the high-order ripple powers flowing among the arms. However, the control of the three-terminal middle cells is complex and the robustness of the topology is relatively weak.

In this article, a modified MMC with active power filter (APF-MMC) topology is presented to reduce the capacitor voltage ripples and power losses of SM. The basic idea is to use two middle SMs to divert the phase ripple powers into the capacitor of the APF circuit, so as to reduce the fluctuations of SM capacitor voltage and arm currents, thus reducing the capacitance value and power losses of the SMs in the MMC system.

The rest of the article is organized as follows. The circuit structure of the APF-MMC topology is introduced in Section II. In Section III, the working principle of the APF circuit is analyzed in detail. Section IV presents the APF-MMC SM capacitor voltage ripples and arm currents. Section V introduces the modulation strategy and control scheme of the APF-MMC topology. In Section VI, the effectiveness of the APF-MMC topology and corresponding control schemes are proved on the simulation and experimental platforms, and the simulations and experimental results are compared with the traditional MMC to show its superiority. Finally, conclusions are summarized in Section VII. In addition, the other types of the APF circuits are discussed in the Appendix.

II. STRUCTURE OF THE PROPOSED APF-MMC

This article proposes an APF-MMC, as shown in Fig. 1. It consists of three-phase legs, each of which includes an upper arm, a lower arm, and an APF circuit. Each arm is composed of a buffer inductor L and N identical SMs, and the APF-MMC can be realized by various kinds of SMs [27]. The Nth SM of the upper arm and the first SM of the lower arm are all called the middle SM (shorten as mid-SM), as shown in Fig. 1. The dc bus and the SMs are connected by the buffer inductor L. The APF circuit is connected in parallel with two mid-SMs, and the APF circuit can be implemented by various kinds of topologies [28], and the comparison results are shown in the Appendix. For simplification, this article just takes a buck-type APF circuit and the half-bridge SMs as an example topology to illustrate the operating principle, and the boost-type APF circuit is also discussed in the Appendix. Each half-bridge SM consists of two IGBTs (T_1 and T_2) with antiparallel diodes (D_1 and D_2) and a capacitor C. The buck-type APF circuit consists of two IGBTs with antiparallel diodes, a buffer inductor L_{dp} and a storage capacitor C_{dp}. In addition, the equivalent series resistance R_0 of the buffer inductor L and L_{dp} is small and can be ignored.

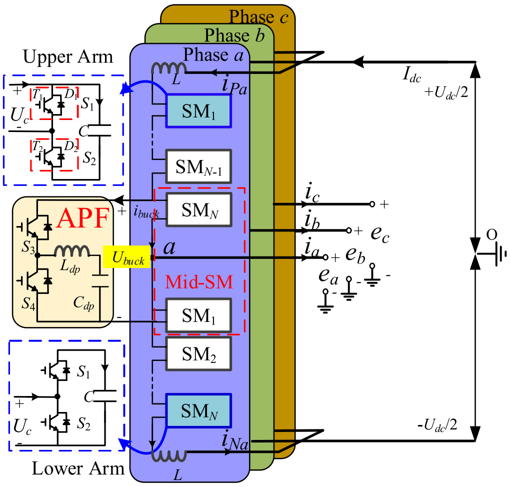

Fig. 1. Configuration of the modified APF-MMC topology.

Assuming that the three-phase output voltages and currents are completely sinusoidal and symmetrical, then the output voltage e_x and current i_x of the APF-MMC can be written as

$$\begin{cases} e_x = E_x \sin(\omega t + \theta_x) \\ i_x = I_x \sin(\omega t + \theta_x - \varphi) \end{cases} \tag{1}$$

where $x = a$, b, and c represents phases a, b, and c, respectively. E_x is the output voltage amplitude, I_x is the output current amplitude, ω is the output frequency, θ_x is the phase angle of the output voltage, and φ is the output power factor angle.

III. WORKING PRINCIPAL OF THE APF-MMC

A. Ripple Powers in the Traditional MMC Topology

In the traditional MMC topology, the voltages u_{Px} and u_{Nx} of the upper and lower arms and the currents i_{Px} and i_{Nx} of the upper and lower arms are, respectively, represented as follows [10]:

$$\begin{cases} u_{Px} = \frac{1}{2} U_{\mathrm{dc}} - e_x \\ u_{Nx} = \frac{1}{2} U_{\mathrm{dc}} + e_x \end{cases} \tag{2}$$

$$\begin{cases} i_{Px} = \frac{1}{3}I_{\mathrm{dc}} + \frac{1}{2}i_x + i_{2f} \\ i_{Nx} = \frac{1}{3}I_{\mathrm{dc}} - \frac{1}{2}i_x + i_{2f} \end{cases} \tag{3}$$

where U_{dc} is the dc bus voltage, I_{dc} is the dc bus current, and i_{2f} is the second-order circulating current.

And the second-order circulating current i_{2f} can be expressed as [28]

$$i_{2f} = I_{2f}\cos(2\omega t + 2\theta_x - \varphi) \tag{4}$$

where I_{2f} is the second-order circulating current amplitude.

According to [30], the mathematical formula of I_{2f} is as follows:

$$I_{2f} = \frac{S}{U_{C\mathrm{ref}}}\sqrt{\frac{9 + k^4\cos^2\varphi - 6k^2\cos^2\varphi}{576\omega^2R_0^2C^2 + \left[48\omega^2LC - N(3 + 2k^2)\right]^2}} \tag{5}$$

where *C* is the capacitance value, *S* is the apparent power of the MMC, *k* is the voltage modulation index, $U_{C\mathrm{ref}}$ is the reference value of the traditional MMC SM, and its relationship with the bus voltage is as follows:

$$U_{C\mathrm{ref}} = \frac{U_{\mathrm{dc}}}{N}. \tag{6}$$

In the traditional MMC topology, the instantaneous power of the upper and lower arms, including SM capacitors powers and arm buffer inductors powers, can be calculated by multiplying the arm voltage by arm current. The results of upper arm power p_{Px} and lower arm power p_{Nx} can be obtained as

$$\begin{cases} p_{Px} = u_{Px}i_{Px} = \frac{U_{\mathrm{dc}}I_{\mathrm{dc}}}{6} - \frac{E_xI_x}{4}\cos\varphi \\ \quad + \frac{U_{\mathrm{dc}}I_x}{4}\sin(\omega t + \theta_x - \varphi) - \frac{E_xI_{\mathrm{dc}}}{3}\sin(\omega t + \theta_x) \\ \quad + \frac{E_xI_{2f}}{2}\sin(\omega t + \theta_x - \varphi) \\ \quad + \frac{U_{\mathrm{dc}}I_{2f}}{2}\cos(2\omega t + 2\theta_x - \varphi) + \frac{E_xI_x}{4}\cos(2\omega t + 2\theta_x - \varphi) \\ \quad - \frac{E_xI_{2f}}{2}\sin(3\omega t + 3\theta_x - \varphi) \\ p_{Nx} = u_{Nx}i_{Nx} = \frac{U_{\mathrm{dc}}I_{\mathrm{dc}}}{6} - \frac{E_xI_x}{4}\cos\varphi \\ \quad - \frac{U_{\mathrm{dc}}I_x}{4}\sin(\omega t + \theta_x - \varphi) + \frac{E_xI_{\mathrm{dc}}}{3}\sin(\omega t + \theta_x) \\ \quad - \frac{E_xI_{2f}}{2}\sin(\omega t + \theta_x - \varphi) \\ \quad + \frac{U_{\mathrm{dc}}I_{2f}}{2}\cos(2\omega t + 2\theta_x - \varphi) + \frac{E_xI_x}{4}\cos(2\omega t + 2\theta_x - \varphi) \\ \quad + \frac{E_xI_{2f}}{2}\sin(3\omega t + 3\theta_x - \varphi). \end{cases} \tag{7}$$

The dc parts of the first two terms in (7) are the powers between the ac and dc side, and the sum of dc parts should be zero to ensure the system stability [26]. Therefore, it can be seen that there are fundamental, second- and third-order harmonics in the arm powers. In addition, it can be seen from (7) that the fundamental and third-order frequency ripple powers are opposite in sign for the upper and lower arms, and the second-order frequency ripple powers are the same in the sign for the upper and lower arms.

As shown in (7), the ripple powers of each phase $p_{x\mathrm{phase}}$ can be calculated by adding the ripple powers of the upper and lower arms, as shown in the following:

$$\begin{aligned} p_{x\mathrm{phase}} &= p_{Px} + p_{Nx} \\ &= \left(U_{\mathrm{dc}}I_{2f} + \frac{E_xI_x}{2}\right)\cos(2\omega t + 2\theta_x - \varphi). \end{aligned} \tag{8}$$

In an MMC topology, energy is transmitted through the SM capacitors. When p_{Px} is positive, the SM capacitors of the upper arm absorb energy. On the contrary, the SM capacitors of the upper arm release energy.

B. Working Principle of the APF Circuit

APFs are developed to compensate the ripple reactive powers and current harmonics [31], such as induction heating systems, electric vehicle battery chargers, and diode rectifiers. The basic working principle of the APF-MMC topology is to control the APF circuit to generate the powers with the opposite phase of $p_{x\mathrm{phase}}$, which is equal to generating an equivalent current i^* opposite to the phase of i_{2f} in the arms. The generated powers by the APF circuit change the circulating current of the APF-MMC, thereby offsetting the phase powers of the traditional MMC and suppressing the SM capacitor voltage ripples. In the APF-MMC topology, in order to ensure the normal operation of the APF circuit, it is necessary to ensure that there is one mid-SM in operation at any time. When the *N*th SM (mid-SM) of the upper arm is put into operation, that is, the dc support voltage of the APF circuit is provided by the mid-SM in the upper arm, the working mode of the APF-MMC is defined as Mode I, as shown in Fig. 2. Similarly, when the first SM of the lower arm (another mid-SM) is put into operation, that is, the dc support voltage of the APF circuit is provided by the mid-SM in the lower arm, the working mode of the APF-MMC is defined as Mode II, as shown in Fig. 3. And in Figs. 2 and 3, SM_t and SM_y represent the SMs that are put into work in the upper and lower arms, while SM_s and SM_z represent the SMs that are bypassed in the upper and lower arms, respectively. i^* is the difference of arm currents between the APF-MMC and the traditional MMC topology, and i_{buck} is the buck current in the APF circuit. The currents i^* and i_{buck}, which are even frequency currents, are calculated in Section IV. And each working mode has four working states. Taking Mode I as an example, the detailed working states are described as follows.

When the phase ripple powers/energy need to be transferred from the MMC to the storage capacitor C_{dp}, switch S_3 is used to control the APF circuit working in the buck phase. During the turn-ON interval of switch S_3, the MMC charges both the buffer inductor L_{dp} and the storage capacitor C_{dp}, as shown in Fig. 2(a), then the even frequency ripple powers of the MMC SMs are offset by the product of the current i^* and the voltage of the corresponding SMs. The buffer inductor L_{dp} will further release its powers/energy to the storage capacitor C_{dp} during the S_3 turn-OFF interval, as shown in Fig. 2(b). If the phase ripple powers/energy need to be released from the storage capacitor C_{dp} back to the MMC, switch S_4 is used to control the APF circuit working in the boost phase. During the turn-ON interval of switch S_4, the buffer inductor L_{dp} is charged by the storage capacitor C_{dp}, as shown in Fig. 2(c). During the turn-OFF interval of switch S_4, both the storage capacitor C_{dp} and buffer inductor L_{dp} will release phase ripple powers/energy back to the MMC, as shown in Fig. 2(d), then the even frequency ripple powers of

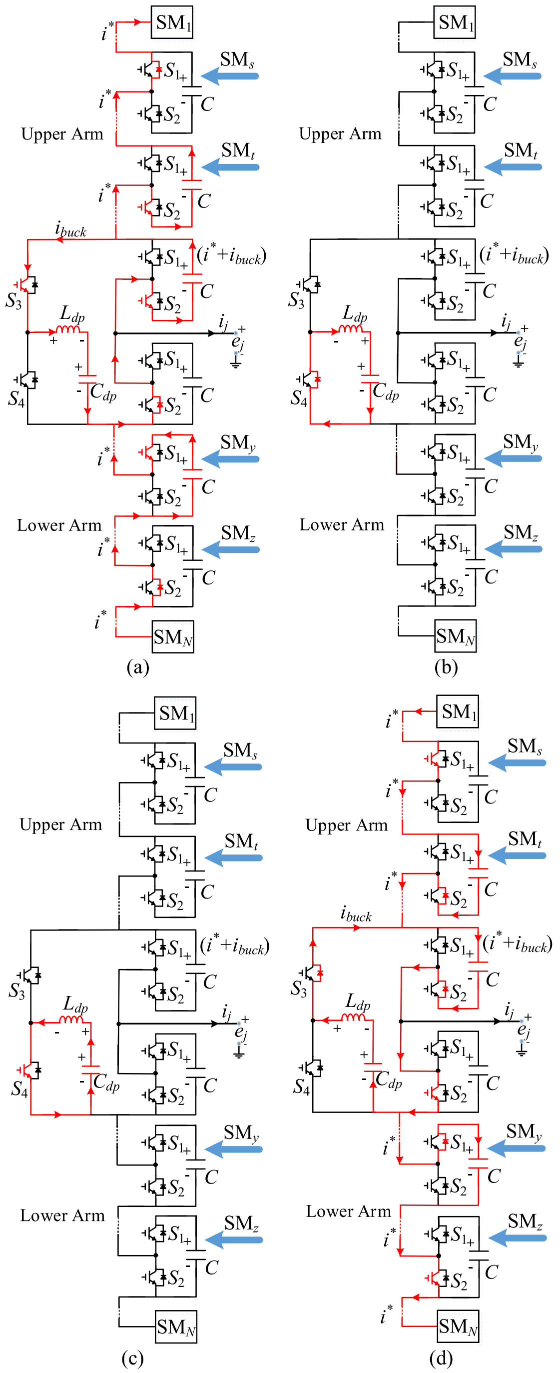

Fig. 2. Four states in working Mode I.

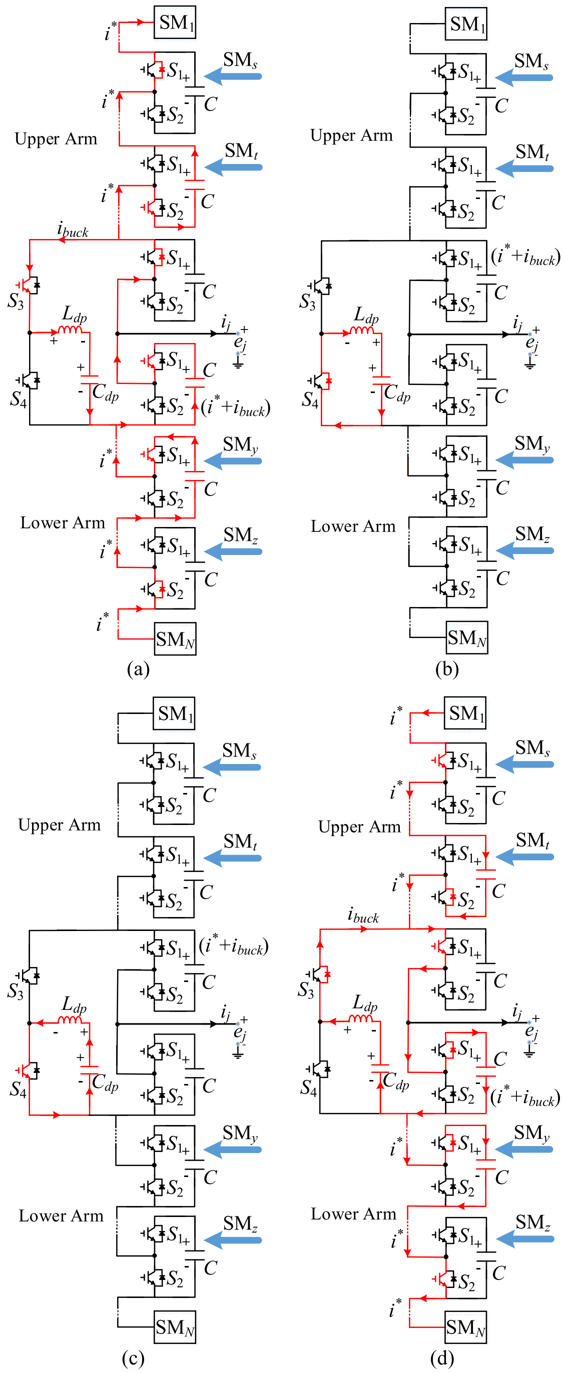

Fig. 3. Four states in working Mode II.

the MMC SMs are counteracted by the product of the current i^* and the voltage of the corresponding SMs.

In addition, due to the special position of the mid-SMs, the even frequency powers of the mid-SMs are disposed by the product of the current $(i^* + i_{\text{buck}})$ and the capacitor voltages of the mid-SMs. And the power change of the mid-SMs will be analyzed in detail in Section IV. The working processes of Mode II, as shown in Fig. 3, are similar to that of Mode I and will not be described in detail.

Based on the analysis of the working modes, the APF circuit can also be connected in parallel to other SMs, but it has a higher voltage rate. In addition, there is no restriction on the operating state of other SMs in each phase, which means no other control complexity is added except for the control of the APF circuit and mid-SMs. What is more, the APF circuit does not reconstruct the traditional MMC topology. And if the APF circuit is moved to the ac side, it will require additional dc sources and zigzag transformer, which increases the hardware cost of the system, and it will have to withstand the higher voltage levels.

The power losses of the parasitic resistances in the buffer inductor L_{dp} and the storage capacitor C_{dp} are small enough to be neglected. In the APF circuit, the energy density of buffer inductor L_{dp} is less than capacitor C_{dp}. Assuming that the inductor L_{dp} works as an energy transfer component that transfers the ripple energy between the capacitor C_{dp} and MMC, and the phase ripple power $p_{x\mathrm{phase}}$ is neutralized by capacitor C_{dp} [32], the following relationship is established:

$$C_{dp}\frac{dv_{dp}}{dt}v_{dp}+p_{x\mathrm{phase}}=0 \tag{9}$$

where v_{dp} is the voltage of the storage capacitor C_{dp}.

Integrating both sides in (9), the energy W_{dp} of the APF storage capacitor C_{dp} can be written as

$$W_{dp}=\frac{1}{2}C_{dp}v_{dp}^2=\int(-p_{x\mathrm{phase}})dt=W_{x\mathrm{phase}}+W_{dp0} \tag{10}$$

where $W_{x\mathrm{phase}}$ is the ripple energy of phase *x*, and W_{dp0} is a constant. The constant W_{dp0} determines the dc offset of v_{dp} and is closely related to the energy storage efficiency [10].

Substituting (8) into (10), the APF storage capacitor voltage v_{dp} and current i_{dp} can be expressed as follows:

$$\begin{aligned}v_{dp}&=\sqrt{\frac{2}{C_{dp}}(W_{x\mathrm{phase}}+W_{dp0})}\\&=\sqrt{\frac{2W_{dp0}}{C_{dp}}-\frac{2U_{\mathrm{dc}}I_{2f}+E_xI_x}{2\omega C_{dp}}\sin(2\omega t+2\theta_x-\varphi)}\end{aligned} \tag{11}$$

$$i_{dp}=-\frac{p_{x\mathrm{phase}}}{v_{dp}}. \tag{12}$$

In the APF-MMC topology, the phase ripple power $p_{x\mathrm{phase}}$ is all absorbed by the APF circuit. Then, the instantaneous powers of the upper and lower arms in the APF-MMC topology can be rewritten as

$$\begin{cases}p_{Px}^{*}=\frac{U_{\mathrm{dc}}I_x}{4}\sin(\omega t+\theta_x-\varphi)+\frac{E_xI_{2f}}{2}\sin(\omega t+\theta_x-\varphi)\\\qquad-\frac{E_xI_{\mathrm{dc}}}{3}\sin(\omega t+\theta_x)-\frac{E_xI_{2f}}{2}\sin(3\omega t+3\theta_x-\varphi)\\p_{Nx}^{*}=-\frac{U_{\mathrm{dc}}I_x}{4}\sin(\omega t+\theta_x-\varphi)-\frac{E_xI_{2f}}{2}\sin(\omega t+\theta_x-\varphi)\\\qquad+\frac{E_xI_{\mathrm{dc}}}{3}\sin(\omega t+\theta_x)+\frac{E_xI_{2f}}{2}\sin(3\omega t+3\theta_x-\varphi)\end{cases} \tag{13}$$

where p_{Px}^{*} is the upper arm ripple power of the APF-MMC topology, and p_{Nx}^{*} is the lower arm ripple power of the APF-MMC topology.

IV. ANALYSIS OF THE PROPOSED TOPOLOGY

A. SM Capacitor Voltage Ripples of the APF-MMC

As can be seen from (13), the ripple powers p_{Px}^{*} and p_{Nx}^{*} only include the fundamental and third-order harmonics' powers, and the signs of the corresponding terms in the expressions of the ripple powers p_{Px}^{*} and p_{Nx}^{*} are opposite. Note that there is no dc power component in the steady state.

Since I_{2f} is much smaller than I_x, the second and fourth items in (13) are all negligible. This article focuses on the fundamental ripple powers, although the APF circuit can also deal with the higher order ripple powers if needed. Neglecting the high-order terms, the two consecutive zero-crossing points of (13) can be calculated as

$$\begin{cases}\omega t_1=\arctan(\frac{m+k}{m-k}\tan\frac{\varphi}{2})-\theta_x+\frac{\varphi}{2}\\\omega t_2=\pi+\arctan(\frac{m+k}{m-k}\tan\frac{\varphi}{2})-\theta_x+\frac{\varphi}{2}\end{cases} \tag{14}$$

where *m* is the current modulation index. The mathematical relationships between *k* and *m* are as follows:

$$\begin{cases}k=\frac{E_x}{U_{\mathrm{dc}}/2}\\m=\frac{I_x/2}{I_{\mathrm{dc}}/3}.\end{cases} \tag{15}$$

The maximum fluctuations of the energy in the upper and lower arms W_{Px} and W_{Nx} can be obtained by integrating the ripple powers of the upper and lower arms between the two consecutive zero-crossing points

$$\begin{cases}W_{Px}=\left|\int_{\omega t_1}^{\omega t_2}p_{Px}(\omega t)d(\omega t)\right|\\=\frac{U_{\mathrm{dc}}I_{\mathrm{dc}}}{3\omega}\left|m\cos(\arctan\psi-\frac{\varphi}{2})-k\cos(\arctan\psi+\frac{\varphi}{2})\right|\\W_{Nx}=\left|\int_{\omega t_1}^{\omega t_2}p_{Nx}(\omega t)d(\omega t)\right|=W_{Px}\end{cases} \tag{16}$$

where

$$\psi=\frac{(m+k)\tan\varphi}{m-k}. \tag{17}$$

Accordingly, the ripple powers in (13) cause SM capacitor voltage ripples. When p_{Px}^{*} or p_{Nx}^{*} is positive, the SM capacitors in the arms absorb energy. On the contrary, the SM capacitors release energy. Therefore, peak-to-peak arm energy variations W_{Px} and W_{Nx} have to be buffered by the *N* SM capacitors in the corresponding arm, that is

$$\begin{aligned}W_{Px}&=\frac{1}{2}NC[U_{C\mathrm{ref}}(1+\varepsilon^{*})]^2-\frac{1}{2}NC_{\mathrm{APF}}[U_{C\mathrm{ref}}(1-\varepsilon^{*})]^2\\&=2NC\varepsilon^{*}U_{C\mathrm{ref}}^2\end{aligned} \tag{18}$$

where ε^{*} is the SM capacitor voltage volatility in the APF-MMC topology.

Based on (16) and (18), ε^{*} can be solved as

$$\varepsilon^{*}=\frac{U_{\mathrm{dc}}I_{\mathrm{dc}}\left|m\cos(\arctan\psi-\frac{\varphi}{2})-k\cos(\arctan\psi+\frac{\varphi}{2})\right|}{6N\omega CU_{C\mathrm{ref}}^2}. \tag{19}$$

In the traditional MMC topology, the capacitance values of SMs are designed to be quite large to restrain the ripple powers [10], and the design formula of SM capacitor voltage volatility ε is as follows [33]:

$$\varepsilon=\frac{U_{\mathrm{dc}}I_{\mathrm{dc}}}{3kN\omega CU_{C\mathrm{ref}}^2}. \tag{20}$$

Based on (19) and (20), with the same electrical parameters and number of SMs, the ratio ρ of the capacitor voltage ripple of the APF-MMC SM compared with that of the traditional MMC SM can be calculated as

$$\rho=\frac{\varepsilon^{*}}{\varepsilon}=\frac{k\left|m\cos(\arctan\psi-\frac{\varphi}{2})-k\cos(\arctan\psi+\frac{\varphi}{2})\right|}{2}. \tag{21}$$

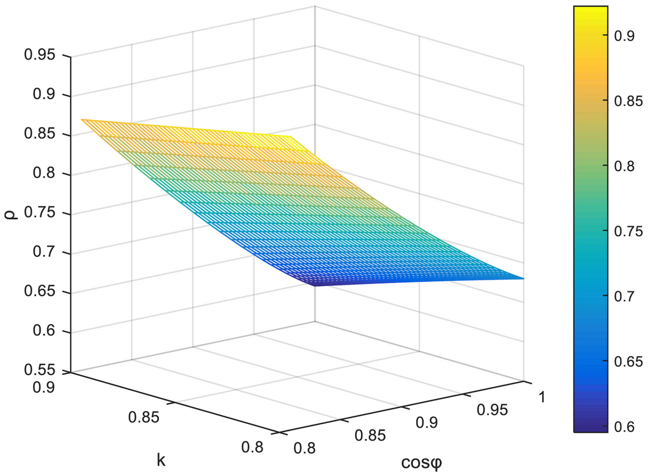

Fig. 4. Effect of voltage modulation index and power factor on the capacitance ratio.

In the HVdc system and offshore wind power system, generally, the voltage modulation index k is assigned around 0.8–0.9 [34], and the power factor ranges from 0.8 to 1 [20]. Fig. 4 shows the voltage ripple ratio ρ against the voltage modulation index k and the power factor angle φ. It can be seen from Fig. 4 that the voltage ripple ratio ρ is less than 1, that is, the SM capacitor voltage fluctuations in the APF-MMC topology are smaller than that in the traditional MMC topology. In addition, according to (21), it can be seen that when $k = 1$ and $\varphi = 0$, the voltage ripple ratio ρ takes the minimum value, which is 1/2, or the SM capacitor voltage ripples of the APF-MMC topology can be reduced up to 50% of the original value in the traditional MMC topology.

B. Voltage Ripple Analysis of APF-MMC SM Capacitors

According to (1), the instantaneous output power of each phase can be calculated as

$$p_x = e_x i_x = \frac{E_x I_x}{2}\cos\varphi - \frac{E_x I_x}{2}\cos(2\omega t + 2\theta_x - \varphi). \tag{22}$$

In the APF-MMC topology, the dc component of the output power p_x is provided by the dc source, that is

$$U_{\rm dc} I^*_{cir1} = \frac{E_x I_x}{2}\cos\varphi \tag{23}$$

where $I* \; cir1$ is the equivalent average current of each phase, and it can be derived as

$$I^*_{cir1} = \frac{kI_x}{4}\cos\varphi. \tag{24}$$

Then, the equivalent average currents of the upper and lower arms can be obtained as

$$\begin{cases} i^*_{P x{\rm eq}} = \frac{kI_x}{4}\cos\varphi + \frac{1}{2}I_x\sin(\omega t + \theta_x - \varphi) \\ i^*_{N x{\rm eq}} = \frac{kI_x}{4}\cos\varphi - \frac{1}{2}I_x\sin(\omega t + \theta_x - \varphi) \end{cases} \tag{25}$$

where $i^*_{Px{\rm eq}}$ is the equivalent average currents of the upper arm, and $i^*_{Nx{\rm eq}}$ is the equivalent average currents of the lower arm.

The equivalent average currents of upper arm SMs $i^*_{PCx{\rm eq}}$ and lower arm SMs $i^*_{NCx{\rm eq}}$ can be calculated as follows [21]:

$$\begin{cases} i^*_{PCx{\rm eq}} = \frac{1}{2}[1 - k\sin(\omega t + \theta_x)]i^*_{Px{\rm eq}} \\ \quad = \frac{I_x}{4}\sin(\omega t + \theta_x - \varphi) - \frac{k^2\cos\varphi I_x}{8}\sin(\omega t + \theta_x) \\ \quad + \frac{kI_x}{8}\cos(2\omega t + 2\theta_x - \varphi) \\ i^*_{NCx{\rm eq}} = \frac{1}{2}[1 + k\sin(\omega t + \theta_x)]i^*_{Nx{\rm eq}} \\ \quad = -\frac{I_x}{4}\sin(\omega t + \theta_x - \varphi) + \frac{k^2\cos\varphi I_x}{8}\sin(\omega t + \theta_x) \\ \quad + \frac{kI_x}{8}\cos(2\omega t + 2\theta_x - \varphi). \end{cases} \tag{26}$$

By integrating (26), the capacitor voltage fluctuations of the upper and lower arms SMs can be obtained as

$$\begin{cases} \Delta u^*_{PCx} = \frac{1}{C}\int_0^t i^*_{PCx{\rm eq}}dt = -\frac{I_x}{4\omega C}\cos(\omega t + \theta_x - \varphi) \\ \quad + \frac{k^2\cos\varphi I_x}{8\omega C}\cos(\omega t + \theta_x) + \frac{kI_x}{16\omega C}\sin(2\omega t + 2\theta_x - \varphi) \\ \Delta u^*_{NCx} = \frac{1}{C}\int_0^t i^*_{NCx{\rm eq}}dt = \frac{I_x}{4\omega C}\cos(\omega t + \theta_x - \varphi) \\ \quad - \frac{k^2\cos\varphi I_x}{8\omega C}\cos(\omega t + \theta_x) + \frac{kI_x}{16\omega C}\sin(2\omega t + 2\theta_x - \varphi) \end{cases} \tag{27}$$

where Δu^*_{PCx} is the capacitor voltage fluctuation value of the upper arm SM, and Δu^*_{NCx} is the capacitor voltage fluctuation value of the lower arm SM. It is observed that the arm SM capacitor voltage ripples mainly contain the fundamental and second-order harmonics.

Accordingly, the second-order item of the output power p_x is supplied by the APF circuit via the mid-SMs, that is

$$U_{\rm buck} I^*_{cir2} = -\frac{E_x I_x}{2}\cos(2\omega t + 2\theta_x - \varphi) \tag{28}$$

where $U_{\rm buck}$ is the input voltage of the APF circuit, and I^*_{cir2} is the equivalent average current for the APF circuit.

To simplify the calculation, assuming $U_{\rm buck}$ is equal to $U_{C{\rm ref}}$, I^*_{cir2} can be derived as

$$I^*_{cir2} = -\frac{NkI_x}{4}\cos(2\omega t + 2\theta_x - \varphi). \tag{29}$$

Then, the equivalent average currents of upper arm mid-SM $i^*_{Pmx{\rm eq}}$ and lower arm mid-SM $i^*_{Nmx{\rm eq}}$ can be calculated as

$$\begin{cases} i^*_{Pmx{\rm eq}} = i^*_{Px{\rm eq}} + I^*_{cir2} = \frac{kI_x}{4}\cos\varphi \\ \quad + \frac{I_x}{2}\sin(\omega t + \theta_x - \varphi) - \frac{NkI_x}{4}\cos(2\omega t + 2\theta_x - \varphi) \\ i^*_{Nmx{\rm eq}} = i^*_{Nx{\rm eq}} + I^*_{cir2} = \frac{kI_x}{4}\cos\varphi \\ \quad - \frac{I_x}{2}\sin(\omega t + \theta_x - \varphi) - \frac{NkI_x}{4}\cos(2\omega t + 2\theta_x - \varphi). \end{cases} \tag{30}$$

Integration of (30) leads to the capacitor voltage fluctuations of mid-SMs Δu^*_{PCmx} and Δu^*_{NCmx} in the upper and lower arm, as in (31) shown at the bottom of the next page.

According to (31) shown at the bottom of the next page, it is observed that the mid-SM capacitor voltage ripples are mainly composed of the fundamental frequency, second-order harmonic, and third-order harmonic.

Similarly, in the traditional MMC topology, the capacitor voltage fluctuations of the upper and lower arms' SMs Δu_{PCx}

and Δu_{NCx} can also be calculated, respectively, that are

$$\begin{cases} \Delta u_{PCx} = \frac{1}{C}\int_0^t \frac{1}{2}[1-k\sin(\omega t+\theta_x)]i_{Px}dt \\ \quad = \frac{k^2\cos\varphi I_x}{8\omega C}\cos(\omega t+\theta_x) - \frac{I_x+kI_{2f}}{4\omega C}\cos(\omega t+\theta_x-\varphi) \\ \quad\quad + \frac{kI_x}{16\omega C}\sin(2\omega t+2\theta_x-\varphi) + \frac{I_{2f}}{4\omega C}\sin(2\omega t+2\theta_x-\varphi) \\ \quad\quad + \frac{kI_{2f}}{12\omega C}\cos(3\omega t+3\theta_x-\varphi) \\ \Delta u_{NCx} = \frac{1}{C}\int_0^t \frac{1}{2}[1+k\sin(\omega t+\theta_x)]i_{Nx}dt \\ \quad = \frac{I_x+kI_{2f}}{4\omega C}\cos(\omega t+\theta_x-\varphi) - \frac{k^2\cos\varphi I_x}{8\omega C}\cos(\omega t+\theta_x) \\ \quad\quad + \frac{kI_x}{16\omega C}\sin(2\omega t+2\theta_x-\varphi) + \frac{I_{2f}}{4\omega C}\sin(2\omega t+2\theta_x-\varphi) \\ \quad\quad - \frac{kI_{2f}}{12\omega C}\cos(3\omega t+3\theta_x-\varphi). \end{cases} \tag{32}$$

In order to simplify the analysis, compared with the traditional MMC topology, the fundamental frequency amplitude change rate η_1 and the second-order harmonic amplitude change rate η_2 of the arm SM capacitor voltage fluctuations in the APF-MMC topology are defined as

$$\begin{cases} \eta_1 = \frac{\frac{I_x}{4\omega C}-\frac{k^2\cos\varphi I_x}{8\omega C}}{\frac{I_x}{4\omega C}-\frac{k^2\cos\varphi I_x}{8\omega C}+\frac{kI_{2f}}{4\omega C}} = \frac{1}{1+\frac{2kI_{2f}}{2I_x-k^2\cos\varphi I_x}} \\ \eta_2 = \frac{\frac{kI_x}{16\omega C}}{\frac{kI_x}{16\omega C}+\frac{I_{2f}}{4\omega C}} = \frac{1}{1+\frac{4I_{2f}}{kI_x}} = \frac{1}{1+\vartheta} \end{cases} \tag{33}$$

where

$$\vartheta = N\cos\varphi\sqrt{\frac{9+k^4\cos^2\varphi-6k^2\cos^2\varphi}{576\omega^2R_0^2C^2+[48\omega^2LC-N(3+2k^2)]^2}}. \tag{34}$$

As can be seen from (33), both the fundamental frequency amplitude change rate η_1 and the second frequency amplitude change rate η_2 are all less than 1. The η_1 and η_2 jointly affect the peak-to-peak value of the SM capacitor voltage ripples, as shown in Fig. 4.

Compared with the traditional MMC topology, the fundamental frequency amplitude change rate γ_1 and the second-order harmonic amplitude change rate γ_2 of the mid-SM capacitor voltage fluctuations in the APF-MMC topology are defined as follows:

$$\begin{cases} \gamma_1 = \frac{\left|\frac{I_x}{4\omega C}-\frac{k^2\cos\varphi I_x}{8\omega C}-\frac{Nk^2I_x}{16\omega C}\right|}{\frac{I_x}{4\omega C}-\frac{k^2\cos\varphi I_x}{8\omega C}+\frac{kI_{2f}}{4\omega C}} = \frac{\left|1-\frac{Nk^2}{4-2k^2\cos\varphi}\right|}{1+\frac{2kI_{2f}}{2I_x-k^2\cos\varphi I_x}} \\ \gamma_2 = \frac{\frac{(N-1)kI_x}{16\omega C}}{\frac{kI_x}{16\omega C}+\frac{I_{2f}}{4\omega C}} = \frac{N-1}{1+\frac{4I_{2f}}{kI_x}} = \frac{N-1}{1+\vartheta}. \end{cases} \tag{35}$$

As can be seen from (35), the fundamental frequency amplitude change rate γ_1 is less than 1, and the second frequency amplitude change rate γ_2 is more than 1. Therefore, the second-order harmonic is the main part of the mid-SM capacitor voltage ripples in the APF-MMC topology.

C. Arm Current Analysis of the APF-MMC Topology

The voltages u_{Px}^* and u_{Nx}^* of the upper and lower arms in the APF-MMC topology are the voltages between the dc bus and the ac output side, which are equal to the voltages of the upper and lower arms of the traditional MMC topology, that are

$$\begin{cases} u_{Px}^* = u_{Px} = \frac{1}{2}U_{\rm dc} - e_x \\ u_{Nx}^* = u_{Nx} = \frac{1}{2}U_{\rm dc} + e_x. \end{cases} \tag{36}$$

The currents i_{Px}^* and i_{Nx}^* of the upper and lower arms that do not contain mid-SMs in the APF-MMC topology are as follows:

$$\begin{cases} i_{Px}^* = i_{Px} - i^* = \frac{1}{3}I_{\rm dc} + \frac{1}{2}i_x + i_{2f} - i^* \\ i_{Nx}^* = i_{Nx} - i^* = \frac{1}{3}I_{\rm dc} - \frac{1}{2}i_x + i_{2f} - i^* \end{cases} \tag{37}$$

where i^* is the difference of arm currents between the APF-MMC topology and the traditional MMC topology.

According to the foregoing analysis, in the APF-MMC topology, the capacitor ripple powers of the upper and lower arms that do not contain the powers of mid-SMs are opposite in sign, and the relationship can be obtained as

$$(u_{Px}^* - u_{Pmx}^*)i_{Px}^* + (u_{Nx}^* - u_{Nmx}^*)i_{Nx}^* = 0 \tag{38}$$

where u_{Pmx}^* and u_{Nmx}^* are the mid-SM capacitor voltages of the upper arm and the lower arm in the APF-MMC topology, respectively.

For the three-phase MMC topology, the total energy stored in the SM capacitors is assumed to be a constant value [26], [35]; hence, the active power of the dc side and the ac side is equal, that is

$$U_{\rm dc}I_{\rm dc} = \frac{3}{2}E_xI_x\cos\varphi. \tag{39}$$

Combining (8) and (36)–(39), i^* can be derived as

$$i^* = \frac{p_{x\rm phase}}{U_{\rm dc}} = \left(I_{2f} + \frac{mkI_{\rm dc}}{6}\right)\cos\left(2\omega t + 2\theta_x - \varphi\right). \tag{40}$$

With (37) and (40), the currents i_{Px}^* and i_{Nx}^* of the upper and lower arms that do not contain mid-SMs in the APF-MMC topology can be obtained as

$$\begin{cases} i_{Px}^* = \frac{I_{\rm dc}}{3} + \frac{I_x}{2}\sin(\omega t+\theta_x-\varphi) \\ \quad\quad - \frac{mkI_{\rm dc}}{6}\cos(2\omega t+2\theta_x-\varphi) \\ i_{Nx}^* = \frac{I_{\rm dc}}{3} - \frac{I_x}{2}\sin(\omega t+\theta_x-\varphi) \\ \quad\quad - \frac{mkI_{\rm dc}}{6}\cos(2\omega t+2\theta_x-\varphi). \end{cases} \tag{41}$$

Comparing (3) with (41), the constant term and the fundamental frequency term of the arm currents in the APF-MMC topology are equal to the corresponding terms in the traditional MMC topology, and the second-order term has changed.

$$\begin{cases} \Delta u_{PCmx}^* = \frac{1}{C}\int_0^t \frac{1}{2}[1-k\sin(\omega t+\theta_x)]i_{Pmx\rm eq}^*dt = \frac{k^2\cos\varphi I_x}{8\omega C}\cos(\omega t+\theta_x) - \frac{(4-Nk^2)I_x}{16\omega C}\cos(\omega t+\theta_x-\varphi) \\ \quad\quad - \frac{(N-1)kI_x}{16\omega C}\sin(2\omega t+2\theta_x-\varphi) - \frac{Nk^2}{48\omega C}\cos(3\omega t+3\theta_x-\varphi) \\ \Delta u_{NCmx}^* = \frac{1}{C}\int_0^t \frac{1}{2}[1+k\sin(\omega t+\theta_x)]i_{Nmx\rm eq}^*dt = \frac{(4-Nk^2)I_x}{16\omega C}\cos(\omega t+\theta_x-\varphi) - \frac{k^2\cos\varphi I_x}{8\omega C}\cos(\omega t+\theta_x) \\ \quad\quad - \frac{(N-1)kI_x}{16\omega C}\sin(2\omega t+2\theta_x-\varphi) + \frac{Nk^2}{48\omega C}\cos(3\omega t+3\theta_x-\varphi) \end{cases} \tag{31}$$

TABLE I
SIMULATION PARAMETERS

Main parameters	**Values**	**Main parameters**	**Values**
Capacity(S)	400kW	Arm inductor(L)	10mH
DC bus voltage(U_{dc})	8000V	APF inductance(L_{dp})	505μH
Number of SMs each arm(N)	8	SM switching frequency(f)	1250Hz
Rated SM capacitor voltage(U_{Cref})	1000V	APF switching frequency(f_{dp})	2kHz
SM capacitance(C_{dp})	1.36mF	Voltage modulation index(k)	0.7778
APF capacitance(C_{dp})	1.36mF	Power factor angle(φ)	0

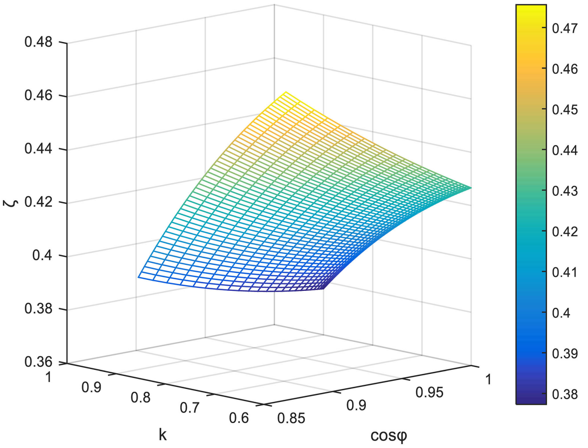

Fig. 5. Proportional relationship between the second-order harmonic component of the APF-MMC arm current and that of the conventional MMC arm current.

The amplitude change rate ζ of the second frequency term can be derived as

$$\xi = \frac{mkI_{\mathrm{dc}}}{6I_{2f}} = \frac{1}{3N\cos\varphi\sqrt{\frac{9+k^4\cos^2\varphi-6k^2\cos^2\varphi}{576\omega^2R_0^2C^2+[48\omega^2LC-N(3+2k^2)]^2}}}. \tag{42}$$

According to (42) and the simulation parameters in Table I, Fig. 5 depicts the proportional relationship between the second-order harmonic component of the APF-MMC arm current and that of the conventional MMC arm current. It can be observed that the second harmonic amplitude of the APF-MMC arm current is smaller than that of the traditional MMC arm current, which further proves that the arm SM capacitor voltage ripples of the APF-MMC topology are smaller than that of the conventional MMC topology.

Assuming that the voltages of the mid-SMs have no fluctuations by the control strategy, and the calculation formula of the buck current i_{buck} in the APF circuit is as follows:

$$\begin{aligned} i_{\mathrm{buck}} &= -\frac{p_{x\mathrm{phase}}}{U_{\mathrm{buck}}} \approx -\frac{p_{x\mathrm{phase}}}{U_{C\mathrm{ref}}} \\ &= -\left(NI_{2f} + \frac{NI_{\mathrm{dc}}}{3\cos\varphi}\right)\cos(2\omega t + 2\theta_x - \varphi). \end{aligned} \tag{43}$$

By subtracting (43) from (41), the current i^*_{Pmx} of the upper arm mid-SM and the current i^*_{Nmx} of the lower arm mid-SM can be calculated as

$$\begin{cases} i^*_{Pmx} = i^*_{Px} - i_{\mathrm{buck}} = \frac{1}{3}I_{\mathrm{dc}} + \frac{1}{2}I_x\sin(\omega t + \theta_x - \varphi) \\ \qquad + [NI_{2f} + \frac{(N-1)I_{\mathrm{dc}}}{3\cos\varphi}]\cos(2\omega t + 2\theta_x - \varphi) \\ i^*_{Nmx} = i^*_{Nx} - i_{\mathrm{buck}} = \frac{1}{3}I_{\mathrm{dc}} - \frac{1}{2}I_x\sin(\omega t + \theta_x - \varphi) \\ \qquad + [NI_{2f} + \frac{(N-1)I_{\mathrm{dc}}}{3\cos\varphi}]\cos(2\omega t + 2\theta_x - \varphi). \end{cases} \tag{44}$$

For the APF-MMC topology, the reference voltages of SMs in the upper and lower arms $u^*_{Px\mathrm{ref}}$ and $u^*_{Nx\mathrm{ref}}$ can be expressed as

$$\begin{cases} u^*_{Px\mathrm{ref}} = \frac{U_{\mathrm{dc}}}{2} - e_x - L\frac{di^*_{Px}}{dt} \\ u^*_{Nx\mathrm{ref}} = \frac{U_{\mathrm{dc}}}{2} + e_x - L\frac{di^*_{Nx}}{dt}. \end{cases} \tag{45}$$

D. Power Losses Analysis of the APF-MMC SM

The power devices' losses are the main components of the APF-MMC topology power losses. And the power devices' losses consist of the conduction losses, switching losses, and blocking losses. The blocking losses are much smaller and can be neglected. The conduction losses are the increasing function of the rms current of IGBT or diode, and the switching losses are the increasing function of the forward average current of IGBT or diode [36].

According to (41), the arm rms current I^*_{rms} of APF-MMC can be calculated as

$$I^*_{\mathrm{rms}} = \sqrt{\frac{I^2_{\mathrm{dc}}}{9} + \frac{m^2I^2_{\mathrm{dc}}}{18} + \frac{m^2k^2I^2_{\mathrm{dc}}}{72}}. \tag{46}$$

Similarly, the arm rms current I_{rms} of the traditional MMC can be solved as

$$I_{\mathrm{rms}} = \sqrt{\frac{I^2_{\mathrm{dc}}}{9} + \frac{m^2I^2_{\mathrm{dc}}}{18} + \frac{I^2_{2f}}{2}}. \tag{47}$$

Comparing (46) with (47), it can obtain that the first two terms are the same, and the third term is different. And the ratio of the third term in (46) and (47) is ζ^2, which means the rms current of APF-MMC SM is smaller than that of the traditional MMC SM, and the conduction losses of the APF-MMC SM are less than that of the traditional SM.

Ignoring the influence of buffer inductors and assuming the phase angle of the output voltage θ_x is 0, when the MMC is operating in the inverter mode, the average current amplitudes of the IGBT $T_{y(y=1,2)}$ and antiparallel diode D_y in the upper arm SM of the traditional MMC topology can be calculated as

$$\begin{cases} I_{T1} = \frac{1}{2\pi}\left|\int_{\varphi}^{\pi+\varphi} i_{Px}\frac{1-k\sin(\omega t+\theta_x)}{2}d\omega t\right| \\ \quad = \frac{2mI_{\mathrm{dc}}+3kI_{2f}}{12\pi} - \frac{kI_{\mathrm{dc}}}{6\pi}\cos\varphi - \frac{kI_{2f}}{12\pi}\cos 2\varphi \\ I_{D1} = \frac{1}{2\pi}\left|\int_{\pi+\varphi}^{2\pi+\varphi} i_{Px}\frac{1-k\sin(\omega t+\theta_x)}{2}d\omega t\right| \\ \quad = \frac{2mI_{\mathrm{dc}}+3kI_{2f}}{12\pi} - \frac{kI_{\mathrm{dc}}}{6\pi}\cos\varphi - \frac{kI_{2f}}{12\pi}\cos 2\varphi \\ I_{D2} = \frac{1}{2\pi}\left|\int_{\varphi}^{\pi+\varphi} i_{Px}\frac{1+k\sin(\omega t+\theta_x)}{2}d\omega t\right| \\ \quad = \frac{I_{\mathrm{dc}}}{6} + \frac{2mI_{\mathrm{dc}}-3kI_{2f}}{12\pi} + \frac{kI_{\mathrm{dc}}}{6\pi}\cos\varphi + \frac{kI_{2f}}{12\pi}\cos 2\varphi \\ I_{T2} = \frac{1}{2\pi}\left|\int_{\pi+\varphi}^{2\pi+\varphi} i_{Px}\frac{1+k\sin(\omega t+\theta_x)}{2}d\omega t\right| \\ \quad = \frac{I_{\mathrm{dc}}}{6} - \frac{2mI_{\mathrm{dc}}-3kI_{2f}}{12\pi} - \frac{kI_{\mathrm{dc}}}{6\pi}\cos\varphi - \frac{kI_{2f}}{12\pi}\cos 2\varphi \end{cases} \tag{48}$$

where I_{T1} is the average current amplitude of the IGBT T_1, I_{T2} is the average current amplitude of the IGBT T_2, I_{D1} and I_{D2} are the average current amplitudes of the freewheeling diodes D_1 and D_2, respectively.

The equivalent average current amplitude $\overline{I}$ in the traditional MMC topology SM can be obtained as

$$\begin{aligned}\overline{I} &= \frac{1}{2}(I_{T1}+I_{T2})+\frac{1}{2}(I_{D1}+I_{D2})\\ &= \frac{I_{\rm dc}}{6}+\frac{2mI_{\rm dc}+3kI_{2f}}{12\pi}-\frac{kI_{\rm dc}}{6\pi}\cos\varphi-\frac{kI_{2f}}{12\pi}\cos 2\varphi.\end{aligned} \tag{49}$$

Similarly, in the upper arm SM of APF-MMC topology, the average current amplitudes of the IGBT T_y^* and antiparallel diode D_y^* can be solved as

$$\begin{cases} I_{T1}^* = \frac{m(4-k^2)I_{\rm dc}}{24\pi}-\frac{kI_{\rm dc}}{6\pi}\cos\varphi+\frac{mk^2I_{\rm dc}}{72\pi}\cos 2\varphi\\ I_{D1}^* = \frac{m(4-k^2)I_{\rm dc}}{24\pi}-\frac{kI_{\rm dc}}{6\pi}\cos\varphi+\frac{mk^2I_{\rm dc}}{72\pi}\cos 2\varphi\\ I_{D2}^* = \frac{I_{\rm dc}}{6}+\frac{m(4+k^2)I_{\rm dc}}{24\pi}+\frac{kI_{\rm dc}}{6\pi}\cos\varphi-\frac{mk^2I_{\rm dc}}{72\pi}\cos 2\varphi\\ I_{T2}^* = \frac{I_{\rm dc}}{6}-\frac{m(4+k^2)I_{\rm dc}}{24\pi}-\frac{kI_{\rm dc}}{6\pi}\cos\varphi+\frac{mk^2I_{\rm dc}}{72\pi}\cos 2\varphi \end{cases} \tag{50}$$

where I_{T1}^* is the average current amplitude of the IGBT T_1^*, I_{T2}^* is the average current amplitude of the IGBT T_2^*, I_{D1}^* and I_{D2}^* are the average current amplitudes of the antiparallel diodes D_1^* and D_2^*, respectively.

The equivalent average current amplitude $\overline{I^*}$ in the APF-MMC topology SM can be derived as

$$\overline{I^*} = \frac{I_{\rm dc}}{6}+\frac{m(4-k^2)I_{\rm dc}}{24\pi}-\frac{kI_{\rm dc}}{6\pi}\cos\varphi+\frac{mk^2I_{\rm dc}}{72\pi}\cos 2\varphi. \tag{51}$$

As a consequence, comparing (49) with (51), one of the significant differences between the traditional MMC topology and the APF-MMC topology is the average current amplitude of SM. And the power losses of SM are proportional to the average current amplitude of the SM [36]. Therefore, the proportion relation τ between the average current I^* of the APF-MMC SM and the average current I of the traditional MMC SM can be calculated as

$$\begin{aligned}\tau &= \frac{\overline{I^*}}{\overline{I}}\\ &= \frac{12\pi I_{\rm dc}+12mI_{\rm dc}-12kI_{\rm dc}\cos\varphi-(3-\cos 2\varphi)mk^2I_{\rm dc}}{12\pi I_{\rm dc}+12mI_{\rm dc}-12kI_{\rm dc}\cos\varphi+(3-\cos 2\varphi)kI_{2f}}.\end{aligned} \tag{52}$$

Fig. 6 shows the average current proportion relation τ against the voltage modulation index k and the power factor angle φ. It can be seen that the average current of SM in the APF-MMC is less than that in the conventional MMC topology, and when $k = 1$ and $\varphi = 0$, it can be reduced up to 87.83% of the original value in the traditional MMC topology.

In summary, the reduction in the average and rms currents means a reduction in the SM power losses, and lower SM power losses are beneficial to the selection and design of heatsink.

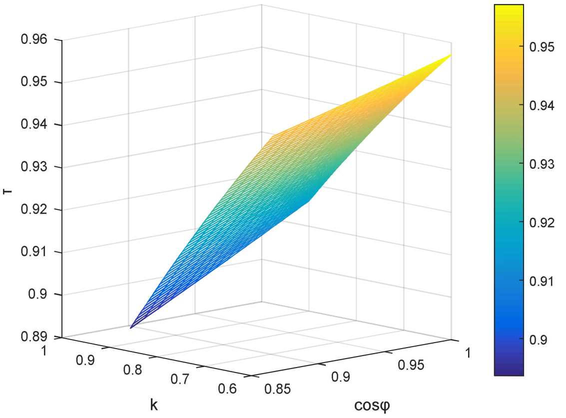

Fig. 6. Average current proportion relation τ against the voltage modulation index k and the power factor angle φ.

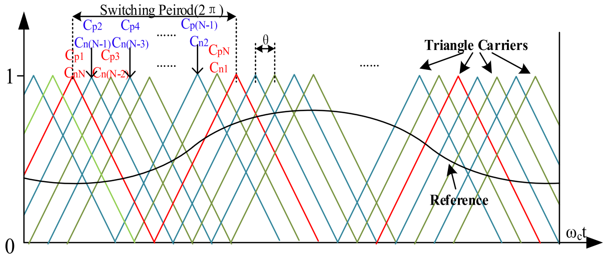

Fig. 7. CPS-SPWM of the APF-MMC.

V. CONTROL SCHEME OF THE APF-MMC

A. Modulation Strategy

sAccording to the working principle of the APF circuit discussed in Section III, one mid-SM has to be put into operation in the APF-MMC topology, which is different from the traditional MMC topology. Therefore, a novel carrier phase-shift sinusoidal pulsewidth modulation (CPS-SPWM) is proposed.

The novel CPS-SPWM for the APF-MMC with N triangular carriers per phase is shown in Fig. 7. The frequency of the triangular carriers is $\omega/2\pi$. The triangular carrier of the gth SM in the upper arm and the $(N + 1 - g)$th SM of the lower arm is the same. And the triangular carriers are equidistantly phase shifted with others by the phase-shift angle: $\theta = 2\pi/N$. Then, the switching pulse signals of each SM are produced by comparing the reference wave with the corresponding triangular carrier wave. When the reference wave is smaller than the carrier wave, switching states of the SM will be “S_1 is OFF and S_2 is ON,” and vice-versa.

B. Control Scheme of the APF-MMC

Due to the different locations of the SMs in the APF-MMC topology, the control objects can be divided into the following three categories:

1) control of the APF circuit;
2) control of the mid-SMs;
3) control of the arm SMs.

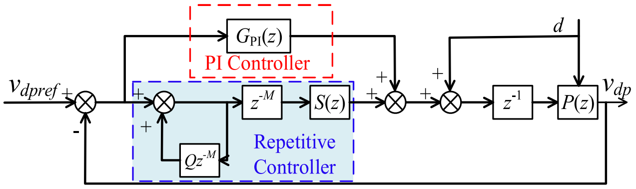

Fig. 8. Novel repetitive controller based on the PI controller.

The control of the arm SMs in the APF-MMC topology is similar to the control of the traditional MMC SMs. Good review of the control technique can be found in [37].

For the APF circuit, the purpose of the controller is to make the voltage of the storage capacitor C_{dp} equal to (11). And the overall control system for the APF storage capacitor voltage should not be included in the phase voltage control.

Because there are the dc and second-order frequency components in the APF storage capacitor reference voltage, a PI controller with faster dynamic response speed is not enough for the accurate reference tracking [10]. A repetitive controller [38] is then considered, which can eliminate the tracking error for the second-order frequency components. But, the output dynamic performance of a repetitive controller is poor. Considering the complementary advantages of the PI controller and repetitive controller, a novel repetitive controller based on the PI controller is proposed, as shown in Fig. 8.

In Fig. 8, *M* is the total sampling intervals, *Q* is an auxiliary compensator, *S*(*z*) is a compensation function designed for the control object, *P*(*z*) is the controlled object, and *d* is a disturbance signal. The transfer function of the PI and repetitive controller *G*(*z*) can be derived as

$$G(z) = \frac{(z^M - Q)G_{\mathrm{PI}}(z)z^{-1}P(z) + S(z)z^{-1}P(z)}{(z^M - Q)(1 + G_{\mathrm{PI}}(z)z^{-1}P(z)) + S(z)z^{-1}P(z)}. \tag{53}$$

For the mid-SMs in the APF-MMC topology, the goal of the controllers is to make the capacitor voltages of the mid-SMs equal to (31). The essential control rule of the mid-SMs is to determine the working modes according to their capacitor voltages and arm current polarity [20].

For the mid-SM in the upper arm, the control block diagram is shown in Fig. 9(a), and the detailed analysis is as follows.

1) If $u^*_{PCmx} > U_{C\mathrm{ref}}$, the mid-SM capacitor should be discharged. If i^*_{Px}>0, the turn-ON time of the IGBT S_1 should be extended, that is, the modulated wave $U_{C\mathrm{ref}}$ is superimposed with a positive correction. And if i^*_{Px}<0, the turn-OFF time of the IGBT S_1 should be extended, that is, the modulated wave $U_{C\mathrm{ref}}$ is superimposed with a negative correction.
2) If $u^*_{PCmx} < U_{C\mathrm{ref}}$, the mid-SM capacitor should be charged. If i^*_{Px}>0, the turn-OFF time of the IGBT S_1 should be extended, that is, the modulated wave $U_{C\mathrm{ref}}$ is superimposed with a negative correction. And if i^*_{Px}<0, the turn-ON time of the IGBT S_1 should be extended, that is, the modulation wave $U_{C\mathrm{ref}}$ is superimposed with a positive correction.

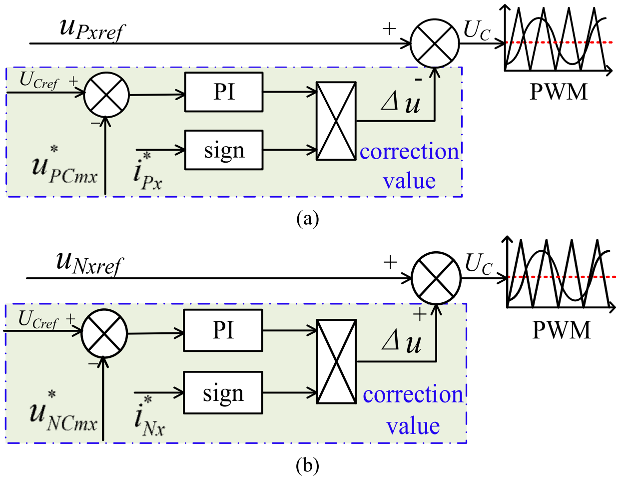

(a)

(b)

Fig. 9. Control block diagram for (a) mid-SM in the upper arm and (b) mid-SM in the lower arm.

For the mid-SM in the lower arm, since its connection mode is symmetrical with the upper arm mid-SM, the sign of the superimposed amount of the modulation wave at the same capacitor voltage is opposite to that of the upper arm mid-SM modulation wave. Similarly, the control block diagram is shown in Fig. 9(b).

According to the above analysis, the voltage references of the mid-SMs can be amended as

$$\begin{cases} u^*_{PCx\mathrm{ref}} = \frac{U_{\mathrm{dc}}}{2} - e_x - u_{Plx} - \mathrm{sign}(i_{Px})(U_{C\mathrm{ref}} - u_{PCmx}) \\ u^*_{NCx\mathrm{ref}} = \frac{U_{\mathrm{dc}}}{2} + e_x - u_{Plx} + \mathrm{sign}(i_{Nx})(U_{C\mathrm{ref}} - u_{NCmx}). \end{cases} \tag{54}$$

VI. Simulations and Experiments

Substituting the data of Table I into (21), the voltage ripple ratio of the SM capacitors ρ can be calculated to be about 0.757. The SM capacitor voltage ripples mainly consist of the fundamental frequency and second-order harmonic components. According to (33), compared with the traditional MMC, the fundamental frequency amplitude change rate η_1 and the second-order harmonic amplitude change rate η_2 of the upper/lower arm SM capacitor voltage fluctuations in the APF-MMC topology are roughly equal to 0.894 and 0.695, respectively. Based on (35), the fundamental frequency amplitude change rate γ_1 and the second frequency amplitude change rate γ_2 of the mid-SM capacitor voltage fluctuations are about 0.119 and 1.194, respectively. Similarly, according to (42), the second frequency amplitude change rate of the arm currents ζ can be calculated to be about 0.420.

A. Simulation Results

Based on the detailed analysis of the APF-MMC topology, single-phase simulation models based on the APF-MMC topology as well as the traditional MMC topology are built in PLECS with detailed parameters listed in Table I.

According to the above analysis, it can be seen that the arm SM capacitor voltages and the mid-SM capacitor voltages are reduced by different proportions, and the results are as follows.

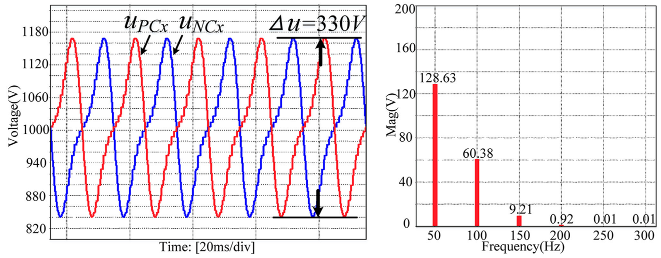

(a) (b)

Fig. 10. Traditional MMC arm SM capacitor voltages and their FFT results.

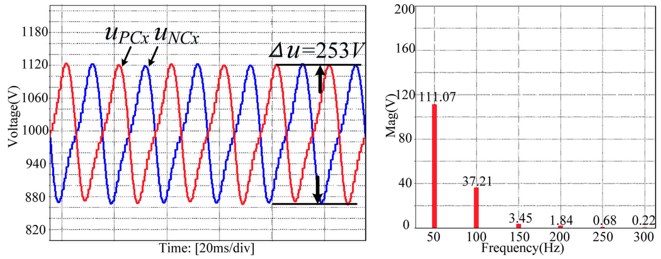

(a) (b)

Fig. 11. APF-MMC arm SM capacitor voltages and their FFT results.

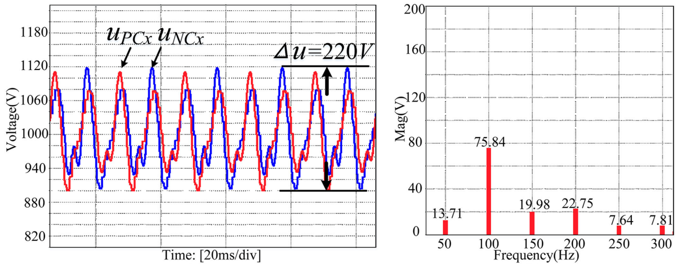

(a) (b)

Fig. 12. APF-MMC arm mid-SM capacitor voltages and their FFT results.

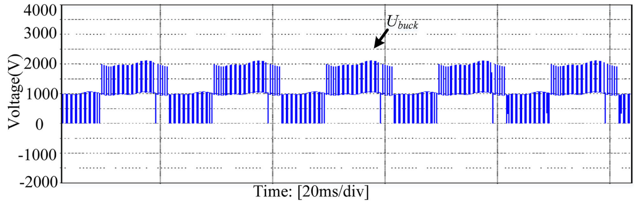

Fig. 13. Input voltage of the APF circuit.

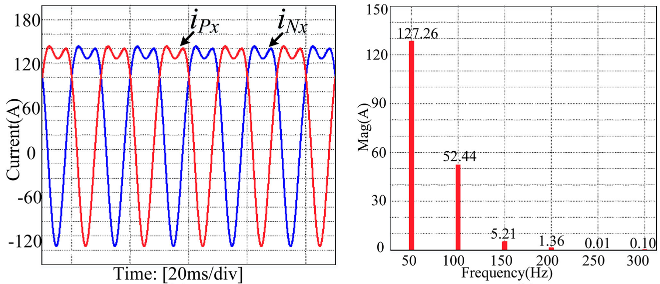

(a) (b)

Fig. 14. Traditional MMC arm currents and their FFT results.

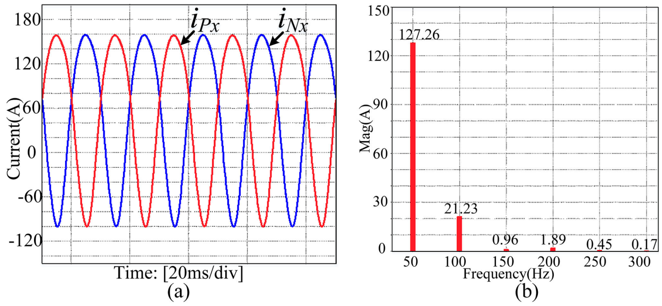

(a) (b)

Fig. 15. APF-MMC arm currents and their FFT results.

Fig. 10(a) shows the SM capacitor voltages of the traditional MMC topology, and the peak-to-peak value is about 330 V. Fig. 11(a) depicts the arm SM capacitor voltages of the APF-MMC topology, and the peak-to-peak value is about 253 V. Obviously, the capacitor voltage ripple of the APF-MMC arm SM is 0.767 times as much as that of the traditional MMC topology, which is close to the theoretical value 0.757. According to (27) and (32), the arm SM capacitor voltage ripples are mainly composed of the fundamental frequency and second-order frequency ripples. Figs. 10(b) and 11(b) show the fast Fourier transform (FFT) analysis results of the arm SM capacitor voltage ripples of the traditional MMC and APF-MMC topology, respectively. It can be calculated from the results that the fundamental frequency amplitude change rate η_1 and the second-order harmonic amplitude change rate η_2 are approximately equal to 0.863 and 0.616, respectively. The capacitor voltage ripples of the APF-MMC mid-SMs and their FFT analysis results are shown in Fig. 12(a) and (b), respectively. It can be calculated from the results that the fundamental frequency amplitude change rate γ_1 and the second frequency amplitude change rate γ_2 are approximately equal to 0.107 and 1.256, respectively. Because U_{buck}, as shown in Fig. 13, takes the approximate value $U_{C\text{ref}}$ in (29), there is a certain error of the second frequency amplitude change rate between the simulation result and theoretical value.

Fig. 14(a) gives the arm currents of the traditional MMC topology, and their FFT analysis results are presented in Fig. 14(b). Fig. 15(a) and (b) shows the arm currents of the APF-MMC topology and their FFT analysis results, respectively. Comparing Fig. 14(b) with Fig. 15(b), it can be seen that compared with the traditional MMC arm current, there is no change in the fundamental frequency of the APF-MMC arm current, and the second-order harmonic has a large reduction. The second frequency amplitude change rate of the arm currents ζ is 0.405.

The transient processes of load changes are shown in Fig. 16. At time t_1, the load decreases from full load to light load; at time t_2, the load returns to the original state. There are no obvious overshoots at the load-change moments, and the APF-MMC system can reach new steady states within several fundamental periods.

In order to prove that the APF-MMC can work well at a low power factor, Figs. 17 and18 present the voltage and current simulation results of the APF-MMC topology and the traditional

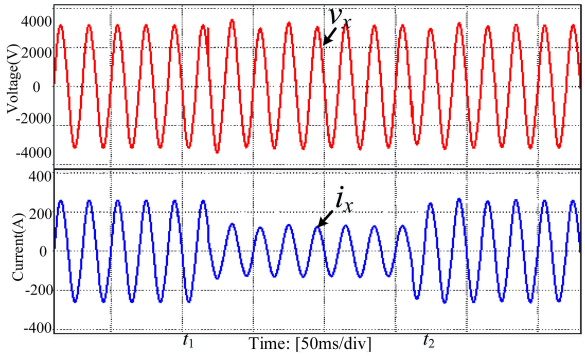

Fig. 16. Output voltage and current of the APF-MMC when the load changes.

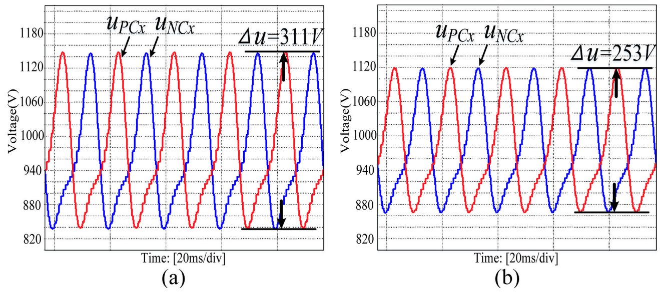

Fig. 17. Capacitor voltages with $\cos\varphi = 0.9$. (a) Traditional MMC. (b) APF-MMC.

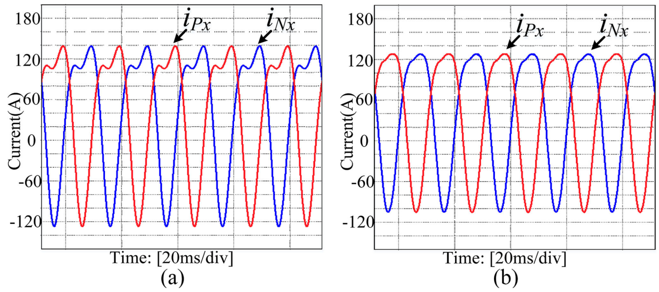

Fig. 18. Arm currents with $\cos\varphi = 0.9$. (a) Traditional MMC. (b) APF-MMC.

MMC topology with $k\approx 0.7778$ and $\cos\varphi = 0.9$. As can be seen from (21), the voltage ripple ratio of the SM capacitors ρ can be calculated to be about 0.808.

The SM capacitor voltages of the traditional MMC topology are shown in Fig. 17(a), and the peak-to-peak value is about 311 V. In contrast, Fig. 17(b) shows the SM capacitor voltages of the APF-MMC, and the peak-to-peak value is about 253 V. It can be calculated that the capacitor voltage ripple of the APF-MMC arm SM is 0.813 times as much as that of the traditional MMC, which is close to the theoretical value 0.798. The arm currents of the traditional MMC and APF-MMC are depicted in Fig. 18(a) and (b), respectively. It is obvious that the arm currents of the APF-MMC are reduced compared with that of the conventional MMC, which means that the SM power losses are reduced.

Figs. 19 and 20 show the voltage and current simulation results of the APF-MMC topology and the traditional MMC topology with $k = 1$ and $\cos\varphi = 1$. The SM capacitor voltages of the traditional MMC and APF-MMC are given in Fig. 19(a) and (b), and the peak-to-peak values are 427 and 215 V, respectively. Obviously, the capacitor voltage ripple of the APF-MMC arm SM is 0.504× as much as that of the traditional MMC topology, which is close to the theoretical value 0.5. In this case, a significant reduction in the capacitor voltage ripples is achieved. Fig. 20(a) shows the arm currents of the traditional MMC, and Fig. 20(b) shows the arm currents of the APF-MMC. By comparing Fig. 20(a) and (b), the arm currents of APF-MMC are smaller than that of the conventional MMC, which means that the SM power losses are decreased.

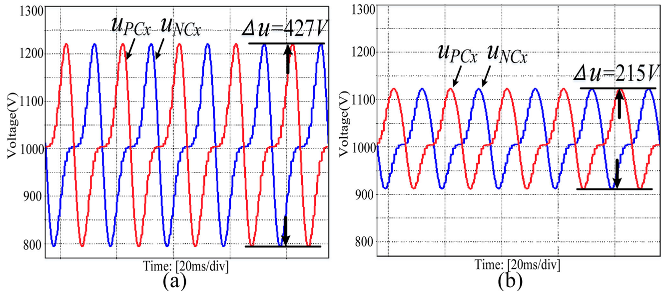

Fig. 19. Capacitor voltages with $k = 1$. (a) Traditional MMC. (b) APF-MMC.

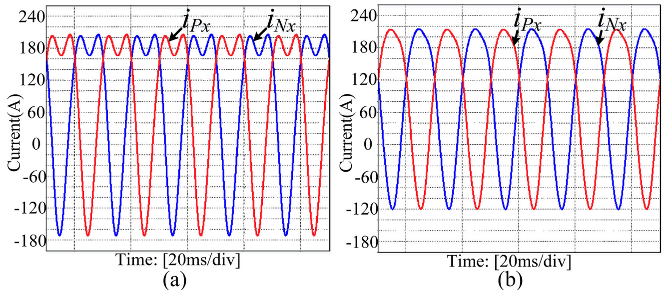

Fig. 20. Arm currents with $k = 1$. (a) Traditional MMC. (b) APF-MMC.

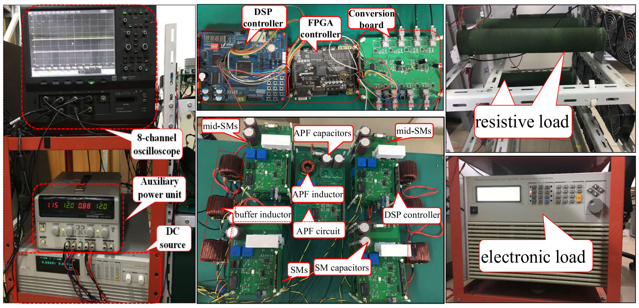

Fig. 21. Pictures of the experimental platform.

B. Experimental Results

To better verifying the effectiveness of the APF-MMC topology and its control strategy, both 1-kW single-phase APF-MMC prototype and a 1-kW single-phase traditional MMC experimental platform were built, as shown in Fig. 21. The prototype includes the power source, measurement tools, control system, and main topology. The control system consists of the DSP

TABLE II
EXPERIMENTAL PARAMETERS

Main parameters	Values	Main parameters	Values
Capacity(S)	1kW	Arm inductor(L)	7mH
DC bus voltage(U_{dc})	400V	APF inductance(L_{dp})	505μH
Number of SMs each arm(N)	4	SM switching frequency(f)	2kHz
Rated SM capacitor voltage(U_{Cref})	100V	APF switching frequency(f_{dp})	2kHz
SM capacitance(C)	1.36mF	Voltage modulation index(k)	0.7778
APF capacitance(C_{dp})	1.36mF	Power factor angle(φ)	0

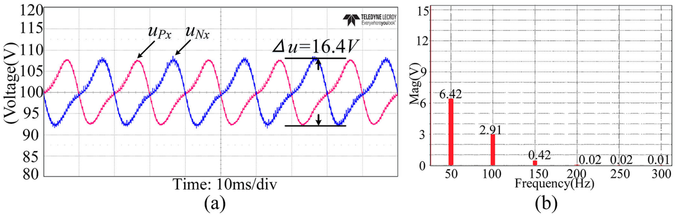

Fig. 22. Traditional MMC arm SM capacitor voltages and their FFT results.

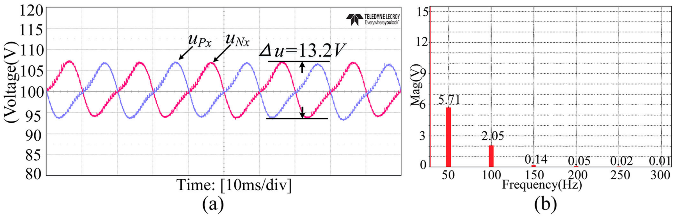

Fig. 23. APF-MMC arm SM capacitor voltages and their FFT results

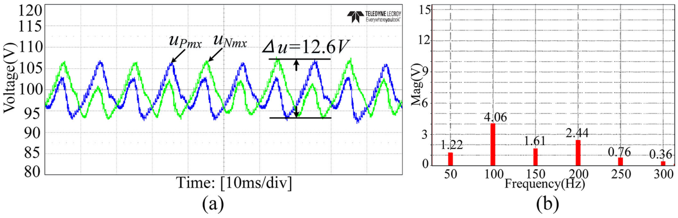

Fig. 24. APF-MMC arm mid-SM capacitor voltages and their FFT results.

(TMS320F28335) + FPGA (EP4CE6F17C8N) main controller and conversion board. And the power switching device used in the SMs is IGBTs, and the part number is IKW25T120FKSA1. The key parameters are listed in Table II.

The detailed experimental results are shown in Figs. 22–33. The arm SM capacitor voltages of the traditional MMC topology are depicted in Fig. 22(a), and the ripple voltage is about 16.4 V. Fig. 22(b) shows the FFT analysis result of the ripple voltage. As analyzed in (32), the ripple voltage mainly consists of the fundamental and second-order harmonics. Fig. 23(a) gives the arm SM capacitor voltages of the APF-MMC topology, and the peak-to-peak value of the ripple voltage is reduced to 13.2 V or 80.5% of the original value. Fig. 23(b) exhibits the FFT analysis result of the ripple voltage of the APF-MMC topology.

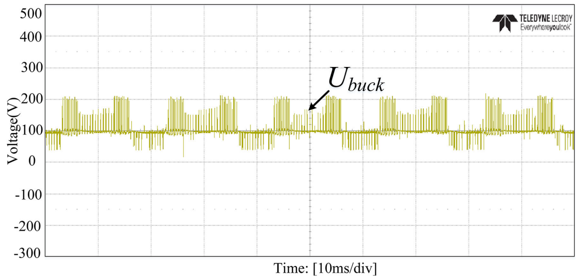

Fig. 25. Input voltage of the APF circuit.

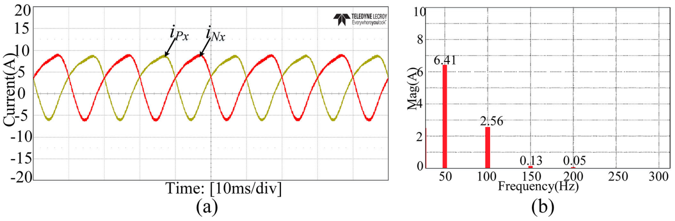

Fig. 26. Traditional MMC arm currents and their FFT results.

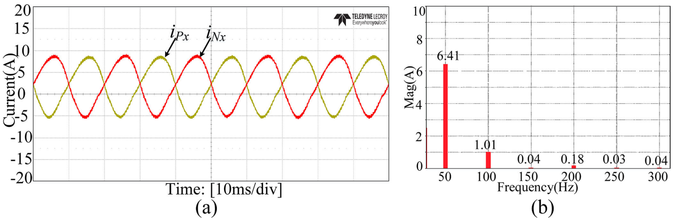

Fig. 27. APF-MMC arm currents and their FFT results.

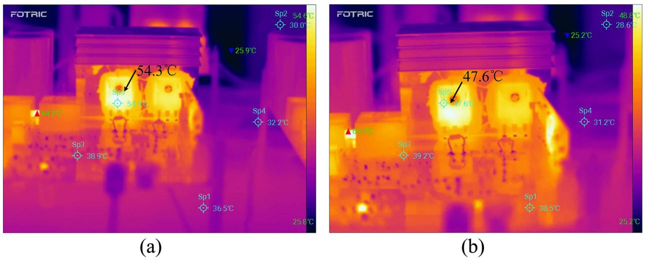

Fig. 28. SM temperature. (a) Traditional MMC. (b) APF-MMC topology.

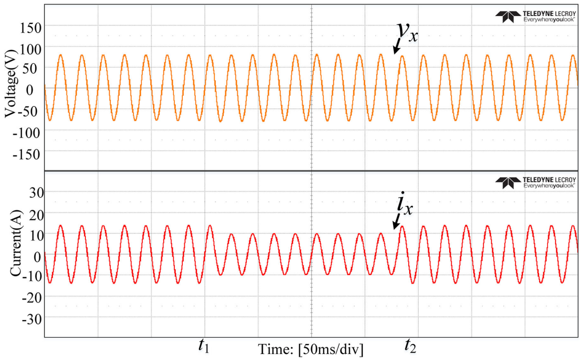

Fig. 29. Output voltage and current of the APF-MMC when the load changes.

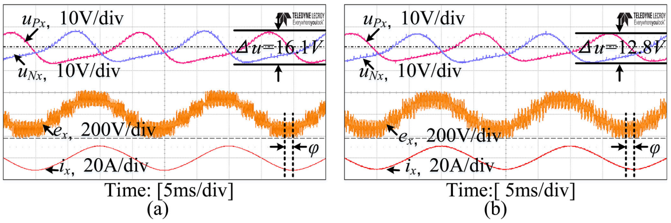

(a) (b)

Fig. 30. Capacitor voltages with cos$\varphi = 0.9$. (a) Traditional MMC. (b) APF-MMC.

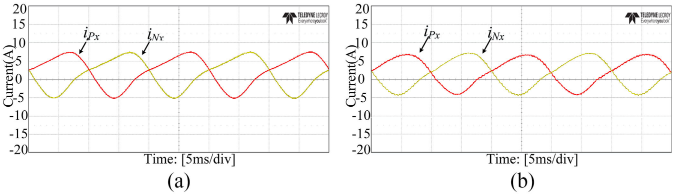

(a) (b)

Fig. 31. Arm currents with cos$\varphi = 0.9$. (a) Traditional MMC. (b) APF-MMC.

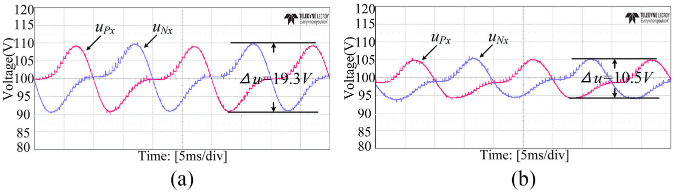

(a) (b)

Fig. 32. Capacitor voltages with $k = 1$. (a) Traditional MMC. (b) APF-MMC.

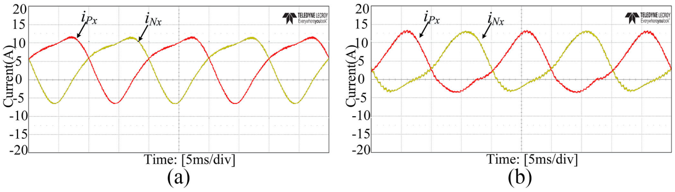

(a) (b)

Fig. 33. Arm currents with $k = 1$. (a) Traditional MMC. (b) APF-MMC.

Compared with the traditional MMC topology, the fundamental frequency amplitude change rate η_1 and the second-order harmonic amplitude change rate η_2 are approximately equal to 0.889 and 0.704, respectively.

Fig. 24(a) shows the mid-SM capacitor voltage ripples of the APF-MMC topology, and the peak-to-peak value of the ripple voltage is about 12.6 V. The FFT analysis results of the mid-SMs are depicted in Fig. 24(b). It can be seen from (31) and Fig. 24(b) that the second-order harmonic in the mid-SM capacitor voltages is the most important part of the ripple voltage. The fundamental frequency amplitude change rate γ_1 and the second frequency amplitude change rate γ_2 are approximately equal to 0.190 and 1.395, respectively. The input voltage of the APF circuit U_{buck} is shown in Fig. 25. In order to simplify the calculation, $U_{C\mathrm{ref}}$ is used in (29) instead of U_{buck}, which leads to a certain error in the second harmonic change rate.

Figs. 26(a) and 27(a) compare the arm currents of the traditional MMC topology with that of the APF-MMC topology. The arm current FFT analysis results of the traditional MMC topology are presented in Fig. 26(b). Fig. 27(b) shows the arm current FFT analysis results of the APF-MMC topology. According to the FFT analysis results, the fundamental frequency component of the APF-MMC topology arm current is the same as that of the traditional MMC topology arm current, but the second harmonic component is greatly reduced, which is 39.4% of the original value. In other words, the second-order frequency amplitude change rate of the arm currents ζ is 0.394. Therefore, the average current amplitude of the APF-MMC topology arm is smaller than that of the traditional MMC topology arm.

As discussed above, the power losses of SM are proportional to the average current amplitude of the SM. It seems that the SM power losses of the APF-MMC topology are less than that of the traditional MMC topology arm. The correctness of the SM power loss analysis is verified by the comparison between the temperature of the SM in the steady-state operation of the traditional MMC topology, as shown in Fig. 28(a), and the temperature of the SM in the steady-state operation of the APF-MMC topology, as shown in Fig. 28(b).

The transient processes of load changes are shown in Fig. 29. At time t_1, the load deceases from full load to light load; at time t_2, the load goes back to the original state. There are no obvious overshoots at the load-change moments, and the APF-MMC system can arrive at new steady states within several fundamental periods.

To further prove that the APF-MMC can work well at a low power factor, the voltage and current experimental results of APF-MMC and traditional MMC with $k \approx 0.7778$ and cos$\varphi = 0.9$ are shown in Figs. 30 and 31, which are analyzed as follows.

The arm SM capacitor voltages of the traditional MMC are depicted in Fig. 30(a), and the ripple voltage is about 16.1 V. As a comparison, Fig. 30(b) presents the capacitor voltages of APF-MMC of which the ripple voltage is about 12.8 V. Comparing Fig. 30(a) with (b), it can be seen that APF-MMC can achieve a reduction in the capacitor voltage fluctuations of about 20%, which matches more or less what is expected according to (21). The arm currents of the traditional MMC and APF-MMC are shown in Fig. 31(a) and (b), respectively. From these values, it can conclude that the SM power losses of APF-MMC are smaller than that of the traditional MMC.

To prove that the capacitor voltage fluctuations can fall up to 50% of the original value, some experiments are carried out. Figs. 31 and 32 show the voltage and current experimental results of the APF-MMC and traditional MMC topology with $k = 1$ and cos$\varphi = 1$. Fig. 32(a) and (b) compares the capacitor voltages of APF-MMC and traditional MMC, and the capacitor voltage fluctuations of APF-MMC is 54.4% of the original value. As can be observed in Fig. 32(a) and (b), a significant reduction in the capacitor voltage ripples is achieved in the APF-MMC topology. The arm currents of the traditional MMC and APF-MMC are depicted in Fig. 33(a) and (b), respectively. The arm currents of APF-MMC are smaller than that of the conventional MMC, which means that the SM power losses are reduced.

Overall, the proposed APF-MMC topology coincides well with the theoretical analysis.

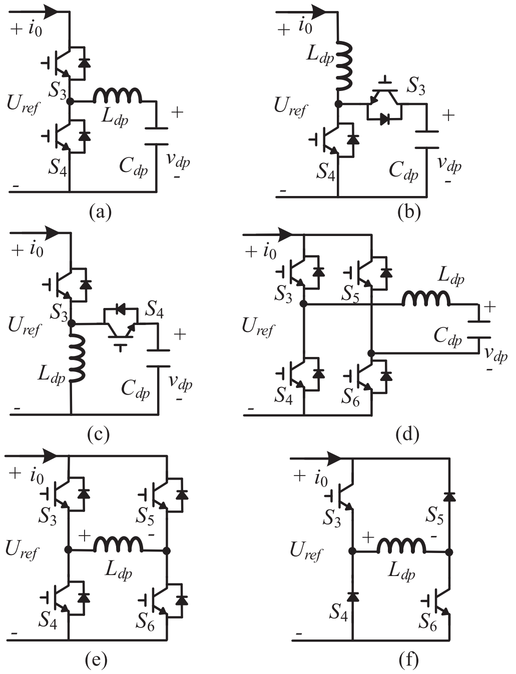

Fig. 34. Various APF circuits. (a) Buck type. (b) Boost type. (c) Buck–boost type. (d) Buck H-bridge type. (e) H-bridge type with an inductor as the energy storage unit. (f) Simplified H-bridge type with an inductor as the energy storage unit.

TABLE III
COMPARISON OF VARIOUS APF CIRCUITS

	Size of passive devices	Voltage of L_{dp}	Current of L_{dp}	Voltage of C_{dp}	Current of C_{dp}
Fig. 33(a)	★★★	★★	★★★	★★	★★★
Fig. 33(b)	★★	★★★	★★	★★★	★★
Fig. 33(c)	Changeable				
Fig. 33(d)	★★★	★★	★★★	★★	★★★
Fig. 33(e)	★★★★	★★★	★★		
Fig. 33(f)	★★★★	★★★	★★		

Note: "⋆" is the unit of quantization.

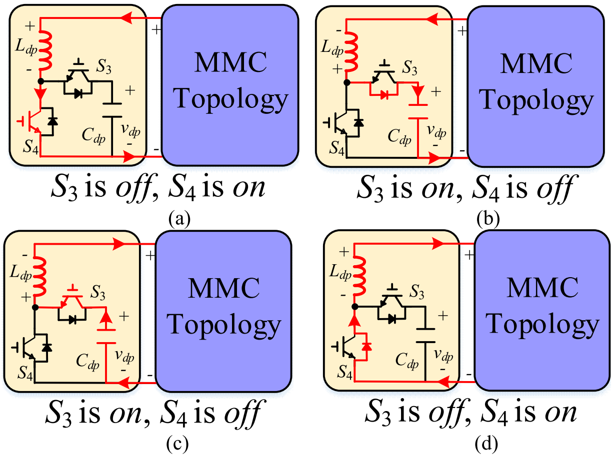

S_3 is *off*, S_4 is *on*
(a)

S_3 is *on*, S_4 is *off*
(b)

S_3 is *on*, S_4 is *off*
(c)

S_3 is *off*, S_4 is *on*
(d)

Fig. 35. Working states of the boost-type APF circuit. (a) S_3 is OFF, S_4 is ON. (b) S_3 is ON, S_4 is OFF. (c) S_3 is ON, S_4 is OFF. (d) S_3 is OFF, S_4 is ON.

VII. CONCLUSION

In this article, a modified APF-MMC topology has been proposed. It inherits the advantages of the traditional MMC topology and only needs to add the APF circuits to the original topology without any other changes. In addition, compared with the traditional MMC topology, it has the following advantages: SM capacitor voltage ripples are smaller and SM power losses are less.

The structure and mathematical model of the APF-MMC topology are introduced, and the SM capacitor voltage ripples and arm currents are also analyzed in detail. Furthermore, its modulation scheme and control strategy are introduced in this article. In addition, the operating modes and the control strategy of the APF circuit are presented. Finally, the simulation platforms and the prototypes of a 1-kW single-phase APF-MMC and a 1-kW single-phase traditional MMC topology are all built and experimentally compared. The simulation and experimental results have proved the availability and the potentiality of the APF-MMC topology and control strategy as a cost-effective scheme for the medium-/high-voltage applications.

APPENDIX

According to the above analysis and the working principle of the APF circuit, the APF circuit can be implemented by other topologies [28], as shown in Fig. 34.

Fig. 34(a) shows a buck-type APF circuit [32], whose voltage and current stresses are analyzed, as outlined above. Due to the voltage polarity constraint, the waveform's sharp of the storage capacitor C_{dp} in the buck-type turns at the bottom and is not smooth, which needs a complex controller [28]. The boost-type APF circuit is analyzed in [39], as shown in Fig. 34(b). And the voltage of the storage capacitor C_{dp} is higher than the terminal voltage U_{ref}. Compared with the buck type, the boost type requires smaller capacitance and current stress, which reduces its volume. And the soft switching of the APF circuit can be implemented through extra resonant inductor and capacitors [40]. However, the capacitor C_{dp} and IGBTs (S_3 and S_4) have to suffer higher voltage stress. Fig. 34(c) depicts a buck–boost-type APF circuit [41], and its storage capacitor voltage has no limitations. Fig. 34(d)–(f) shows three different H-bridge-type APF circuits of which Fig. 34(e) and (f) uses inductors as energy storage elements [42]. Due to the low power density of the inductor, H-bridge types with an inductor as the energy storage unit have a large size [32].

According to the article presented in [28], Table III presents the comparison results of the sizes, voltage, and current stresses of capacitors and inductors in various APF circuits. To minimize the size of the storage capacitor C_{dp}, the boost-type APF circuit can be used instead of the buck-type APF circuit, as shown in Fig. 35. The working states are briefly analyzed as follows.

In the boost-type APF circuit, the capacitor C_{dp} is used as the energy storage component, and the inductor L_{dp} works as the energy transfer component that transfers the ripple energy/powers between the capacitor C_{dp} and the MMC. When the ripple energy/powers need to be transferred from the MMC to the capacitor C_{dp}, switch S_4 is used to control the APF circuit working in the boost phase. During the turn-ON interval of switch S_4, the MMC charges the buffer inductor L_{dp}, as shown in Fig. 35(a). The inductor L_{dp} will release its energy/powers to the storage capacitor C_{dp} during the S_4 turn-OFF interval, as shown in Fig. 35(b). If the ripple energy/powers need to be released from the storage capacitor C_{dp} back to the MMC, switch S_3 is used to control the APF circuit working in the buck phase. During the turn-ON interval of switch S_3, the buffer inductor L_{dp} is charged by the storage capacitor C_{dp}, as shown in Fig. 35(c). During the turn-OFF interval of S_3, the inductor L_{dp} will release energy/powers back to the MMC, as shown in Fig. 35(d). Then, the currents of inductor L_{dp} and capacitor C_{dp} can be obtained as

$$\begin{cases} i_{Ldp} = -\frac{p_{x\text{phase}}}{U_{\text{ref}}} \\ i_{Cdp} = -\frac{p_{x\text{phase}}}{v_{dp}}. \end{cases} \tag{55}$$

In (55), the storage capacitor voltage v_{dp} is higher than the terminal voltage U_{ref}. Compared with the buck-type APF circuit, the boost type has smaller capacitance and capacitor current, which reduces its size. However, the capacitor C_{dp} and IGBTs (S_3 and S_4) have to suffer higher voltage stress.

Based on the aforementioned analysis, the APF circuit generally chooses a buck-type or boost-type topology, and this article selects a buck-type APF circuit in the APF-MMC topology.

REFERENCES

[1] P. Hu, R. Teodorescu, S. Wang, S. Li, and J. M. Guerrero, “A currentless sorting and selection-based capacitor-voltage-balancing method for modular multilevel converters,” *IEEE Trans. Power Electron.*, vol. 34, no. 2, pp. 1022–1025, Feb. 2019.

[2] J. Rodriguez *et al.*, “Multilevel converters: An enabling technology for high-power applications,” *Proc. IEEE*, vol. 97, no. 11, pp. 1786–1817, Nov. 2009.

[3] Z. Zhang, Z. Xu, and Y. Xue, “Valve losses evaluation based on piecewise analytical method for MMC–HVDC links,” *IEEE Trans. Power Del.*, vol. 29, no. 3, pp. 1354–1362, Jun. 2014.

[4] A. Lesnicar and R. Marquardt, “An innovative modular multilevel converter topology suitable for a wide power range,” in *Proc. IEEE Bologna Power Tech. Conf.*, Bologna, Italy, Jun. 23–26, 2003, vol. 3, p. 6.

[5] R. Marquardt, “Modular multilevel converter: An universal concept for HVDC-networks and extended DC-bus-applications,” in *Proc. Int. Power Electron. Conf.*, 2010, pp. 502–507.

[6] S. Debnath, J. Qin, B. Bahrani, M. Saeedifard, and P. Barbosa, “Operation control and applications of the modular multilevel converter: A review,” *IEEE Trans. Power Electron.*, vol. 30, no. 1, pp. 37–53, Jan. 2015.

[7] K. Friedrich, “Modern HVdc PLUS application of VSC in modular multilevel converter topology,” in *Proc. IEEE Int. Symp. Ind. Electron.*, Nov. 2010, pp. 3807–3810.

[8] S. P. Teeuwsen, “Modeling the trans bay cable project as voltage-sourced converter with modular multilevel converter design,” in *Proc. IEEE Power Energy Soc. Gen. Meeting*, 2011.

[9] Q. Song, W. Liu, X. Li, H. Rao, S. Xu, and L. Li, “A steady-state analysis method for a modular multilevel converter,” *IEEE Trans. Power Electron.*, vol. 28, no. 8, pp. 3702–3713, Aug. 2013.

[10] Z. Kong, X. Huang, Z. Wang, J. Xiong, and K. Zhang, “Active power decoupling for submodules of a modular multilevel converter,” *IEEE Trans. Power Electron.*, vol. 33, no. 1, pp. 125–136, Jan. 2018.

[11] A. J. Korn, M. Winkelnkemper, and P. Steimer, “Low output frequency operation of the modular multi-level converter,” in *Proc. IEEE Energy Convers. Congr. Expo.*, 2010, pp. 3993–3997.

[12] R. Picas, J. Pou, S. Ceballos, V. G. Agelidis, and M. Saeedifard, “Minimization of the capacitor voltage fluctuations of a modular multilevel converter by circulating current control,” in *Proc. 38th Annu. Conf. IEEE Ind. Electron. Soc.*, Montreal, QC, Canada, Oct. 25–28, 2012, pp. 4985–4991.

[13] J. Pou, S. Ceballos, G. Konstantinou, V. G. Agelidis, R. Picas, and J. Zaragoza, “Circulating current injection methods based on instantaneous information for the modular multilevel converter,” *IEEE Trans. Ind. Electron.*, vol. 62, no. 2, pp. 777–788, Feb. 2015.

[14] S. P. Engel and R. W. De Doncker, “Control of the modular multilevel converter for minimized cell capacitance,” in *Proc. 14th Euro. Conf. Power Electron. Appl.*, Birmingham, U.K., Aug. 30–Sep. 1, 2011, pp. 1–10.

[15] R. Picas, J. Pou, S. Ceballos, J. Zaragoza, G. Konstantinou, and V. G. Agelidis, “Optimal injection of harmonics in circulating currents of modular multilevel converters for capacitor voltage ripple minimization,” in *Proc. IEEE ECCE Asia Downunder*, 2013, pp. 318–324.

[16] J. Pou, S. Ceballos, G. Konstantinou, G. J. Capella, and V. G. Agelidis, “Control strategy to balance operation of parallel connected legs of modular multilevel converters,” in *Proc. IEEE Int. Symp. Ind. Electron.*, 2013.

[17] M. Vasiladiotis, N. Cherix, and A. Rufer, “Accurate capacitor voltage ripple estimation and current control considerations for grid-connected modular multilevel converters,” *IEEE Trans. Power Electron.*, vol. 29, no. 9, pp. 4568–4579, Sep. 2014.

[18] M. Winkelnkemper, A. Korn, and P. Steimer, “A modular direct converter for transformerless rail interties,” in *Proc. IEEE Int. Symp. Ind. Electron.*, 2010, pp. 562–567.

[19] S. Zhou, B. Li, M. Guan, X. Zhang, Z. Xu, and D. Xu, “Capacitance reduction of the hybrid modular multilevel converter by decreasing average capacitor voltage in variable-speed drives,” *IEEE Trans. Power Electron.*, vol. 34, no. 2, pp. 1580–1594, Feb. 2019.

[20] K. Wang, Y. Li, Z. Zheng, and L. Xu, “Voltage balancing and fluctuation suppression method of floating capacitors in a new modular multilevel converter,” *IEEE Trans. Ind. Electron.*, vol. 60, no. 5, pp. 1943–1954, May 2013.

[21] B. Li, Y. Zhang, G. Wang, W. Sun, D. Xu, and W. Wang, “A modified modular multilevel converter with reduced capacitor voltage fluctuation,” *IEEE Trans. Ind. Electron.*, vol. 62, no. 10, pp. 6108–6119, Oct. 2015.

[22] L. He, K. Zhang, J. Xiong, S. Fan, X. Chen, and Y. Xue, “New modular multilevel converter with power channels between upper- and lower arms suitable for MV drives,” in *Proc. IEEE Appl. Power Electron. Conf. Expo.*, 2015, pp. 799–805.

[23] S. Du, B. Wu, K. Tian, N. R. Zargari, and Z. Cheng, “An active cross-connected modular multilevel converter (AC-MMC) for a medium-voltage motor drive,” *IEEE Trans. Ind. Electron.*, vol. 63, no. 8, pp. 4707–4717, Aug. 2016.

[24] S. Du, B. Wu, and N. R. Zargari, “A star-channel modular multilevel converter for zero/low-fundamental-frequency operation without injecting common-mode voltage,” *IEEE Trans. Power Electron.*, vol. 33, no. 4, pp. 2857–2865, Apr. 2018.

[25] S. Sau and B. G. Fernandes, “Modular multilevel converter based variable speed drive with reduced capacitor ripple voltage,” *IEEE Trans. Ind. Electron.*, vol. 66, no. 5, pp. 3412–3421, May 2019.

[26] H. Ming, J. Zou, X. Ma, Y. Li, and M. Han, “Modified modular multilevel converter to reduce sub-module capacitor voltage ripples without common-mode voltage injected,” *IEEE Trans. Ind. Electron.*, vol. 66, no. 3, pp. 2236–2246, Mar. 2019.

[27] S. Debnath, J. Qin, B. Bahrani, M. Saeedifard, and P. Barbosa, “Operation, control, and applications of the modular multilevel converter: A review,” *IEEE Trans. Power Electron.*, vol. 30, no. 1, pp. 37–53, Jan. 2015.

[28] Y. Sun, Y. Liu, M. Su, W. Xiong, and J. Yang, “Review of active power decoupling topologies in single-phase systems,” *IEEE Trans. Power Electron.*, vol. 31, no. 7, pp. 4778–4794, Jul. 2016.

[29] Q. Tu, Z. Xu, H. Huang, and J. Zhang, “Parameter design principle of the arm inductor in modular multilevel converter based HVDC,” in *Proc. Int. Conf. Power Syst. Technol.*, 2010.

[30] Y. Zhou, D. Jiang, J. Guo, P. Hu, and Y. Liang, “Analysis and control of modular multilevel converters under unbalanced conditions,” *IEEE Trans. Power Del.*, vol. 28, no. 4, pp. 1986–1995, Oct. 2013.

[31] H. Vahedi, A. A. Shojaei, L.-A. Dessaint, and K. Al-Haddad, “Reduced DC-link voltage active power filter using modified PUC5 converter,” *IEEE Trans. Power Electron.*, vol. 33, no. 2, pp. 943–947, Feb. 2018.

[32] R. Wang *et al.*, “A high power density single-phase PWM rectifier with active ripple energy storage,” *IEEE Trans. Power Electron.*, vol. 26, no. 5, pp. 1430–1443, May 2011.

[33] H. Yang, W. Li, L. Lin, and X. He, “Decoupled current control with synchronous frequency damping for MMC considering sub-module capacitor voltage ripple,” *IEEE Trans. Power Del.*, vol. 33, no. 1, pp. 419–428, Feb. 2018.

[34] B. Li *et al.*, "An improved circulating current injection method for modular multilevel converters in variable-speed drives," *IEEE Trans. Ind. Electron.*, vol. 63, no. 11, pp. 7215–7225, Nov. 2016.

[35] K. Ilves, A. Antonopoulos, S. Norrga, and H.-P. Nee, "Steady-state analysis of interaction between harmonic components of arm and line quantities of modular multilevel converters," *IEEE Trans. Power Electron.*, vol. 27, no. 1, pp. 57–68, Jan. 2012.

[36] B. Masserant and T. Stuart, "Experimental verification of calculated IGBT losses in PFCs," *IEEE Trans. Aerosp. Electron. Syst.*, vol. 32, no. 3, pp. 1154–1158, Jul. 1996.

[37] A. Nami, J. Liang, F. Dijkhuizen, and G. D. Demetriades, "Modular multilevel converters for HVDC applications: Review on converter cells and functionalities," *IEEE Trans. Power Electron.*, vol. 30, no. 1, pp. 18–36, Jan. 2015.

[38] L. He, K. Zhang, J. Xiong, and S. Fan, "A repetitive control scheme for harmonic suppression of circulating current in modular multilevel converters," *IEEE Trans. Power Electron.*, vol. 30, no. 1, pp. 471–481, Jan. 2015.

[39] S. Wang, X. Ruan, K. Yao, S.-C. Tan, Y. Yang, and Z. Ye, "A flicker-free electrolytic capacitor-less AC–DC LED driver," *IEEE Trans. Power Electron.*, vol. 27, no. 11, pp. 4540–4548, Nov. 2012.

[40] H. Zhang, X. Li, B. Ge, and R. S. Balog, "Capacitance, dc voltage utilization, and current stress: Comparison of double-line frequency ripple power decoupling for single-phase systems," *IEEE Ind. Electron. Mag.*, vol. 11, no. 3, pp. 37–49, Sep. 2017.

[41] X. Cao, Q.-C. Zhong, and W.-L. Ming, "Ripple eliminator to smooth DC-bus voltage and reduce the total capacitance required," *IEEE Trans. Power Electron.*, vol. 62, no. 4, pp. 2224–2235, Apr. 2015.

[42] T. Larsson and S. Ostlund, "Active DC link filter for two frequency electric locomotives," *Proc. Int. Conf. Electr. Railways United Eur.*, Amsterdam, The Netherlands, 1995, pp. 97–100.

Guanlong Jia (Student Member, IEEE) received the B.S. degree from Xinjiang University, Urumqi, China, in 2014, and the M.S. degree from Tianjin University, Tianjin, China, in 2017. He is currently working toward the Ph.D. degree in electrical engineering with Zhejiang University, Hangzhou, China.

His research interests include multilevel converters, high-power electronics, control algorithms, and pulsewidth modulation techniques.

Min Chen (Member, IEEE) received the B.S. degree in applied electronics and the Ph.D. degree in electrical engineering from Zhejiang University, Hangzhou, China, in 2000 and 2006, respectively.

From 2007 to 2009, he was a Postdoctoral Researcher with the Department of Electrical Engineering, Zhejiang University, where he has been a Lecturer since 2010, and is currently an Associate Professor. From 2014 to 2015, he was a Visiting Researcher with the Department of Energy Technology, Aalborg University. Since 2007, he has been responsible for the Lighting Research and Development Laboratory, National Engineering Research Center for Applied Power Electronics. He is currently the Vice Director of the National Key Laboratory of Power Electronics, and the Director of Zhejiang Joint research Center for New Energy and Power Electronics Based Power System. He has authored or coauthored more than 60 technical papers. He has been issued for 19 Chinese patents and one U.S. Patent. His research interests include power electronics in power system, inverter system, photovoltaic system and microinverter, electrical vehicle, regenerative energy system, distributed generation, energy storage system, and modern lighting system for HID lamps and LED.

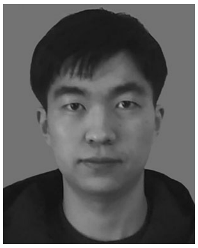

Song Tang (Student Member, IEEE) received the B.S. degree from Shanghai Jiao Tong University, Shanghai, China, in 2018. He is currently working toward the Ph.D. degree with Zhejiang University, Hangzhou, China.

His research interests include modular multilevel converter, dc circuit breaker, and HVdc fault protection techniques.

Chenghao Zhang received the B.S. degree in 2019 from Zhejiang University, Hangzhou, China, where he is currently working toward the M.S. degree.

His research interests include multilevel converters and control algorithms.

Bin Zhao received the B.E. degree in electrical engineering from Central South University, Changsha, China, in 2017. He is currently working toward the master's degree with the College of Electrical Engineering, Zhejiang University, Hangzhou, China.

His research interests include microgrid system, emergency power source, application of power electronics in power system, and renewable energy.